



THE UNIVERSITY *of* EDINBURGH

Edinburgh Research Explorer

Stall-induced fatigue damage in nonlinear aeroelastic systems under stochastic inflow

Citation for published version:

Tripathi, D, Vishal, S, Bose, C & Venkatramani, J 2022, 'Stall-induced fatigue damage in nonlinear aeroelastic systems under stochastic inflow: Numerical and experimental analyses', *International journal of non-Linear mechanics*, vol. 142, 104003. <https://doi.org/10.1016/j.ijnonlinmec.2022.104003>

Digital Object Identifier (DOI):

[10.1016/j.ijnonlinmec.2022.104003](https://doi.org/10.1016/j.ijnonlinmec.2022.104003)

Link:

[Link to publication record in Edinburgh Research Explorer](#)

Document Version:

Peer reviewed version

Published In:

International journal of non-Linear mechanics

General rights

Copyright for the publications made accessible via the Edinburgh Research Explorer is retained by the author(s) and / or other copyright owners and it is a condition of accessing these publications that users recognise and abide by the legal requirements associated with these rights.

Take down policy

The University of Edinburgh has made every reasonable effort to ensure that Edinburgh Research Explorer content complies with UK legislation. If you believe that the public display of this file breaches copyright please contact openaccess@ed.ac.uk providing details, and we will remove access to the work immediately and investigate your claim.



Stall-induced fatigue damage in nonlinear aeroelastic systems under stochastic inflow: numerical and experimental analyses

Dheeraj Tripathi^a, Sai Vishal^a, Chandan Bose^b, J Venkatramani^{a,*}

^a*Department of Mechanical Engineering, Shiv Nadar University, India*

^b*School of Engineering, Institute for Energy Systems, University of Edinburgh, United Kingdom*

Abstract

This study focuses on characterizing the fatigue damage accumulated in nonlinear aeroelastic systems subjected to stochastic inflows through both numerical simulations and wind tunnel experiments. In the mathematical model, nonlinearities are assumed to exist either in the structure (via a cubic hardening nonlinearity in the pitch stiffness), or in the flow (via dynamic stall condition), or simultaneously in both the structural and aerodynamic counterparts. The aerodynamic loads in the attached flow and dynamic stall conditions are estimated using Wagner's formulation and semi-empirical Leishman-Beddoes model, respectively. To augment the findings to in-field flow conditions, the oncoming wind flow is considered to be randomly time-varying in nature. The stochastic input flow fluctuations are modeled using a Karhunen-Loeve Expansion formulation. The response dynamics and the associated fatigue damage of the aeroelastic system, possessing different sources of nonlinearities, are systematically investigated under isolated cases of deterministic and stochastic input flows. Specifically, the pertinent role of stochasticity in the input flow is brought out by presenting the response dynamics and the associated fatigue damage accumulation for different values of noise intensity and time scale of the input flow fluctuation. It is demonstrated that under fluctuating flow conditions, the dynamics intermittently switch between attached flow and the dynamic stall regimes even at low mean flow speeds. The intermittent nature of the response varies as the time scale and intensity of the oncoming flow are varied. The role of torsional stresses as the predominant component dictating the fatigue damage accumulation irrespective of the source of nonlinearity is illustrated. Using the rainflow counting method and Miner's linear damage accumulation theory, it is shown that the accumulated fatigue damage is substantially higher under stochastic flow conditions as compared to deterministic input flows. Importantly, it is observed that different time scales and intensities of the oncoming flow fluctuation play a pivotal role in dictating the fatigue damage in aeroelastic systems. Finally, fatigue damage is observed to be significantly higher for torsionally dominant oscillations in the dynamical stall regime compared to the oscillations at the attached flow regime. The numerical findings are strengthened by drawing comparisons with the preliminary results obtained from wind tunnel experiments performed on a NACA 0012 airfoil undergoing dynamic stall. To the best of our knowledge, this is the first study that systematically bridges the dichotomy between the stall induced dynamical signatures in stochastic aeroelastic systems and maps the same to the corresponding structural damage.

Keywords: Dynamic stall, Stochastic flow, Fatigue damage, Rainflow counting algorithm, Aeroelastic flutter, Wind tunnel experiments

1. Introduction

Safe design of aeroelastic systems, such as wind turbine blades and helicopter rotor blades often needs to consider the coupled nonlinear interactions of the elastic and inertial forces of the structure with the unsteady aerodynamic loads. A ubiquitous dynamic phenomenon observed in aeroelastic

*Corresponding author

Email address: j.venkatramani@snu.edu.in (J Venkatramani)

5 structures is flutter instability that occurs due to a continuous energy transfer between the struc-
6 ture and the surrounding flow-field. In the presence of nonlinearities in the structure and/or flow,
7 phenomenologically rich bifurcation behavior in the system response is observed [1], which in turn
8 can potentially jeopardize the structural safety of the underlying aeroelastic system [2]. The charac-
9 teristics of these dynamical responses and the route to flutter have been extensively studied in the
10 literature **by considering a continuous aeroelastic system or a canonical two degrees-of-**
11 **freedom (DoF) pitch-plunge aeroelastic system [3]. The continuous aeroelastic system**
12 **can be modelled in different ways such as beam model, shell model etc. [4] and can be**
13 **solved using finite element based solvers [4, 5, 6]. However, the simplified 2-DoF pitch-**
14 **plunge aeroelastic model is more commonly used for flutter prediction and is faster and**
15 **reasonably accurate [3, 7].** Flutter instability in nonlinear aeroelastic systems is marked by the
16 onset of self-sustained Limit Cycle Oscillations (LCOs), typically via a Hopf bifurcation. Under the
17 assumption of the attached flow condition, linear aerodynamic models can predict the dynamical
18 signatures with sufficient accuracy. However, at higher values of instantaneous angles-of-attack, the
19 linear approximations become insufficient with the onset of the dynamic stall phenomenon, involving
20 nonlinear wake effects due to flow separation and vortex shedding [1].

21 Dynamic stall is commonly encountered in high angle-of-attack applications, such as wind tur-
22 bine blades, turbomachinery blades, and helicopter blades. An aeroelastic instability occurring at
23 this regime, known as stall flutter, gives rise to large-amplitude pitch-dominated self-sustained oscil-
24 lations [8]. Aeroelastic analysis of nonlinear structures under dynamic stall conditions has attracted
25 widespread attention in the recent literature [9, 10, 11, 12, 8]. The bifurcation route to stall flutter
26 [9, 10] and the stall flutter characteristics have been thoroughly investigated for different structural
27 configurations, and sources of nonlinearity [11, 12]. Sai Vishal *et al.* [13] showed that a pitch-plunge
28 aeroelastic system subjected to dynamic stall conditions could exhibit stall or classical flutter re-
29 sponse - depending on the particular route to synchronization. It is worth noting the fact that
30 most of these studies are carried out assuming uniform flow conditions. However, in actual field
31 conditions, aerodynamic loads on structures like wind turbines and helicopter rotor blades are often
32 highly stochastic in nature due to the variation of flow speed with time and/or height in the atmo-
33 spheric boundary layer. Recent studies by Bethi *et al.* [14], and Devathi and Sarkar [15] highlight
34 the significance of adopting a stochastic flow model and studying the subsequent impact on the
35 aeroelastic response dynamics. The authors have shown the presence of noise-induced intermittency
36 (NII) even at low mean flow speeds, triggered due to the input flow fluctuations. In a recent study,
37 dos Santos and Marques [16] showed that, depending on the intensity of flow fluctuations, the aeroe-
38 lastic structures enter high amplitude stall flutter regimes, and the probability of reaching divergent
39 oscillations increases rapidly, even at speeds below the linear flutter boundary.

40 Aeroelastic structures exhibiting stall flutter oscillations at high angles-of-attack have been spec-
41 ulated to be more susceptible to fatigue-induced failure as compared to classical flutter [17, 18].
42 A distinct trait of stall flutter is the torsional dominance in the high-amplitude LCOs [7]. Most
43 materials used in the engineering applications are prone to failures due to torsional stresses [19],
44 necessitating an in-depth investigation of the structures exhibiting stall flutter from the standpoint
45 of structural health monitoring. Additionally, the impact of stall-induced oscillations (as well as
46 classical flutter oscillations) in the presence of stochastic inflow on structural damage has received
47 less attention in the aeroelastic literature. This can be attributed to the fact that failure deter-
48 mination due to the aging effects such as fatigue accumulation is a challenging problem to date
49 due to the uncertainties associated with the time-varying loads. Although the studies on fatigue
50 damage for constant and variable amplitude loading and associated crack growth mechanisms have
51 been performed for various aeroelastic applications like suspension bridges [20], wind turbines [19],
52 aircrafts [21], similar studies addressing the effects of structural and aerodynamic nonlinearities are
53 limited [22, 19] in hitherto literature. Sarkar *et al.*[22] investigated the fatigue damage induced in
54 a randomly vibrating 1-DoF aeroelastic system in the presence of fluctuating flow under dynamic
55 stall conditions using the ONERA model. Although the authors demonstrated the impact of flow
56 uncertainty on fatigue damage, the aeroelastic structure was modeled using a rather simplistic 1-DoF
57 model. Further, the impact of the discontinuous nonlinearity arising from dynamic stall conditions
58 was not investigated due to the ONERA aerodynamic model's limitations. Venkatesh *et al.*[19] in-
59 vestigated the effect of uncertainties on the fatigue damage of wind turbine blades and noted that

60 random flow fluctuations pose a greater threat to the structural integrity as compared to parametric
61 uncertainty. However, the flow was considered attached, and hence, does not incorporate the effects
62 of aerodynamic nonlinearity associated with the flow separation. In light of these studies, the present
63 paper aims to investigate the effect of stochastic inflow on nonlinear pitch-plunge aeroelastic systems
64 from the standpoint of structural safety.

65 It is worth noting that the hitherto studies, be it for dynamics or fatigue damage analysis, have
66 considered either a low-order 1-DoF structural model and a semi-empirical dynamic stall aerody-
67 namic model [22] or a 2-DoF structural model with linear aerodynamic model [19]. However, a
68 2-DoF airfoil model gives rise to rich dynamical signatures that the 1-DoF model does not capture.
69 Galvanetto *et al.*[10] reports aperiodic oscillations in the bifurcation characteristics of a 2-DoF aeroe-
70 lastic system under the stall. Similar observations entailing a period-doubling route to chaos were
71 noted by Sarkar and Bijl[9] in a 2-DoF aeroelastic system subjected to dynamic stall. On the other
72 hand, only a transition to LCOs via a Hopf bifurcation is reported in typical 1-DoF stall flutter
73 problem [23]. Furthermore, the hitherto literature on aeroelastic fatigue damage studies does not
74 consider the combined effect of coupled structural and aerodynamic nonlinearities that can give rise
75 to radically different response dynamics compared to isolated nonlinearities, either in the structure
76 or in the aerodynamics [24]. Furthermore, the presence of random input flow fluctuations may sig-
77 nificantly alter the bifurcation scenario and result in the loss of stability under critical conditions
78 [25, 26, 27]. Therefore, the incurred fatigue damage in these scenarios will be qualitatively and
79 quantitatively distinct from that reported in the existing literature. To that end, structural health
80 monitoring of in-field aeroelastic systems demands a systematic investigation under the combined
81 effect of structural and aerodynamic nonlinearities with the additional complexity of random input
82 flows. A comparative study of the fatigue damage induced in the cases of coupled nonlinearities
83 with that of the isolated cases is essential. Similarly, comparing damage values obtained in scenarios
84 involving deterministic flows against stochastic input flow fluctuations can provide crucial insights
85 into the structural safety of nonlinear aeroelastic systems under gusty conditions. Furthermore, the
86 role of probabilistic markers such as noise intensity and time scales of the input flow behind the
87 fatigue damage accumulation is not clear in terms of triggering NII [25]. **Indeed, typical flexible
88 structures such as unmanned aerial vehicles (UAVs) [28], wind turbine blades [29], and
89 helicopter blades [30] are often subjected to dynamic stall, hand-in-hand with stochas-
90 tically fluctuating wind loads. While the ability of aeroelastic systems to display large
91 amplitude periodic oscillations (often LCOs) has motivated the community to estimate
92 fatigue damage incurred using RFC [22, 19], the ability of noise-induced dynamical
93 signatures like intermittency to incur fatigue damage in aeroelastic systems remains
94 unanswered. In wake of low-flow applications like wind turbine blade etc to be sub-
95 jected to both noisy wind flow and dynamic stall behavior, attempting to present the
96 safety of noise-induced responses in stochastic stall flutter problems is an immediate
97 need.** To the best of the authors' knowledge, there have been minimal efforts to systematically
98 document the role of coupled structural and aerodynamic nonlinearities and input flow fluctuations
99 (and its probabilistic markers) hand-in-hand behind the incurred fatigue damage. The present study
100 is devoted to taking up this analysis.

101 In this study, a 2-DoF pitch-plunge aeroelastic system subjected to randomly fluctuating loads is
102 considered that exhibits flutter oscillations, arising either under attached flow (linear aerodynamics)
103 or dynamic stall conditions (nonlinear aerodynamics). The accumulated fatigue damage in the
104 structure is compared in these two scenarios. The structure is assumed to possess a cubic hardening
105 nonlinearity in the pitch DoF unless stated otherwise. The nonlinear aerodynamic loads at high
106 angles-of-attacks during stall flutter are calculated using the Leishman-Beddoes (LB) semi-empirical
107 dynamic stall model [31], and the loads in the attached flow regimes (which in turn give rise to
108 classical flutter) are calculated using Wagner's function-based unsteady formulation. The random
109 fluctuations in the flow are incorporated using the Karhunen-Loeve Expansion (KLE) formulation
110 [25]. The response dynamics of the system at attached flow and dynamic stall regimes for flow speeds
111 lying below and above the linear flutter boundary are systematically laid out for both deterministic
112 and stochastic inflow scenarios. As a first step to investigate the fatigue damage from the earlier
113 investigated aeroelastic responses, the locations of maximum stress applied on the airfoil geometry,
114 referred to as critical points, are identified. Then, the corresponding stress cycles are calculated

115 using the rainflow counting (RFC) algorithm [32]. The RFC algorithm can model random stress
 116 cycles that arise, essentially due to the NII signatures of the response dynamics, and is widely
 117 used for estimating fatigue damage in most engineering applications. Finally, the linear damage
 118 accumulation rule developed by Miner [33], based on Palmgren’s linear accumulation theory [34], is
 119 combined with the RFC algorithm to obtain the cumulative fatigue damage induced in the airfoil for
 120 both classical and stall flutter cases. Finally, the findings are compared against nonlinear aeroelastic
 121 scenarios involving deterministic flows. In a nutshell, the focal points of the present study are as
 122 follows: (i) to investigate the effect of coupled structural and aerodynamic nonlinearity on response
 123 dynamics of the aeroelastic structure under fluctuating inflow, (ii) to analyze the effect of the time
 124 scales of oncoming flow on aeroelastic responses, and iii) to compare the resultant fatigue damage
 125 in structure due to different sources of nonlinearity under different time scales of fluctuating inflow.

126 The rest of this paper is organized in the following sections. Section 2 depicts the mathematical
 127 formulation of structural equations, aerodynamic loads, the stochastic model used to incorporate
 128 the random fluctuations in the flow, and the methodology deployed to compute the fatigue damage.
 129 Section 3 presents a comparison of the aeroelastic responses at attached flow and dynamic stall
 130 regimes for deterministic and stochastic cases. Section 4 details the methods used to calculate the
 131 critical points and stress cycles. Then, the estimated fatigue loads for the corresponding cases,
 132 investigated in Section 3, are presented. A preliminary experimental investigation into stall induced
 133 oscillations and corresponding fatigue damage analysis is presented in Section 5. Finally, the salient
 134 findings of the study are summarized in Section 6. **To summarize the objectives of this work,
 135 a schematic illustrating the outline of the problem with the methodology and the end-
 136 outcome of fatigue damage is presented in Fig. 1.**

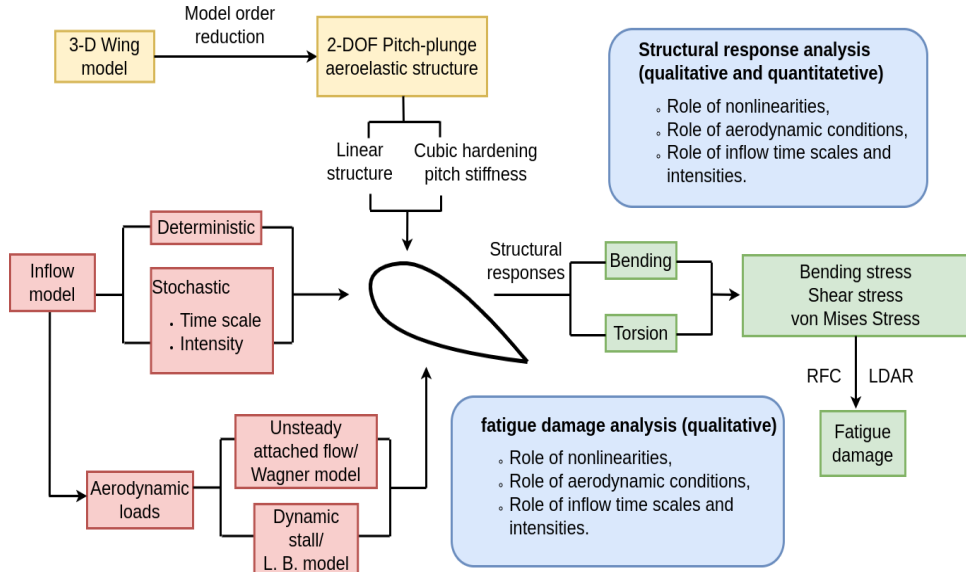


Figure 1: Schematic representation of the work-flow involved in this study.

137 2. Mathematical model of the aeroelastic system

138 2.1. Structural model

139 A 2-DoF aeroelastic system, exhibiting pitch (α) and plunge (ξ) motion through the torsional
 140 and translational springs, respectively, is considered for the present study. The schematic of the
 141 representative airfoil-spring system is shown in Fig. 2. Here, $b = c/2$ denotes the semi-chord length,
 142 where c is the chord-length. a_h is the nondimensional length of mid-chord from the elastic axis,
 143 and x_α is the nondimensional length of the mass center from the elastic axis; both the lengths are
 144 considered to be positive towards the trailing edge and are nondimensionalized with the value of b .
 145 k_ξ and k_α represent bending and torsional stiffness, respectively. The structural damping is assumed

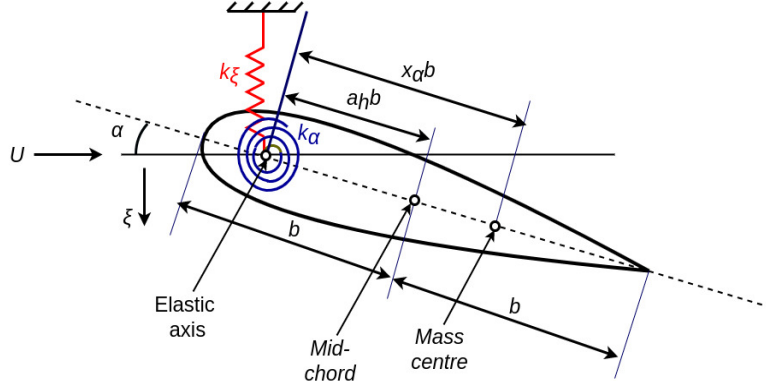


Figure 2: Schematic representation of the pitch-plunge aeroelastic system. The airfoil section is considered to be NACA 0012.

146 to be zero in the present study [3]. For a 2-DoF pitch-plunge aerofoil, the equations of motion in
 147 the nondimensional form are given by [3]

$$\xi'' + x_\alpha \alpha'' + \left(\frac{\bar{\omega}}{U}\right)^2 \xi = -\frac{1}{\pi\mu} C_l(\tau), \quad (1)$$

$$\frac{x_\alpha}{r_\alpha^2} \xi'' + \alpha'' + \left(\frac{1}{U}\right)^2 (\alpha + \beta_\alpha \alpha^3) = \frac{2}{\pi\mu r_\alpha^2} C_m(\tau). \quad (2)$$

148 Here, $\xi = h/b$ is the nondimensional plunge displacement, where h denotes the dimensional plunge
 149 deflection and is positive in downward direction. α is the nondimensional pitch angle about the elastic
 150 axis, considered to be positive at nose up. $\bar{\omega}$ is the ratio of the dimensional natural frequencies of
 151 plunge (ω_ξ) and pitch (ω_α). $U = V/b\omega_\alpha$ is the nondimensional flow speed, where V is the dimensional
 152 free-stream velocity. $\mu = m_a/\pi\rho b^2$ represents the nondimensional mass ratio, where m_a is the airfoil
 153 mass and ρ is the density of the air. The pitch and plunge stiffness in their nondimensional form
 154 are represented as a function of their respective displacements.

155 To compare the fatigue damage accumulation between a linear and a nonlinear aeroelastic system,
 156 a linear and a cubic hardening stiffness in the pitch DoF are considered, respectively. A generic
 157 function representing the pitch stiffness is provided in Eq. 2, where β_α is the nondimensional coefficient
 158 of cubic stiffness in pitch. It should be noted that β_α value becomes zero when the system
 159 is linear. The plunge stiffness is considered to be linear throughout the study. $\tau = Vt/b$ is the
 160 nondimensional time, where t is the dimensional time and r_α represents the nondimensional radius
 161 of gyration about the elastic axis given by $r_\alpha = \sqrt{I_\alpha/m_a b^2}$, where I_α is the moment of inertia
 162 about pitch. C_l and C_m denote the aerodynamic lift and moment coefficients, respectively. The
 163 mathematical formulation to estimate the aerodynamic load coefficients is presented in the following
 164 subsection.

165 2.2. Aerodynamic model

166 The present study investigates the response dynamics and the corresponding fatigue damage of
 167 the system under attached flow and dynamic stall conditions. The aerodynamic load coefficients
 168 under attached flow conditions, considering the flow to be inviscid and incompressible, the lift and
 169 moment coefficients are estimated using Wagner's unsteady aerodynamic formulation in the time
 170 domain [3]. The expression to obtain the load coefficients is given by,

$$C_l(\tau) = \pi(\xi'' - a_h \alpha'' + \alpha') + 2\pi[\alpha(0) + \xi'(0) + (0.5 - a_h)\alpha'(0)]\phi(\tau) + 2\pi \int_0^\tau \phi(\tau - \tau_0)[\alpha'(\tau_0) + \xi''(\tau_0) + (0.5 - a_h)\alpha''(\tau_0)]d\tau_0, \quad (3)$$

$$\begin{aligned}
C_m(\tau) = & \pi(0.5 + a_h)[\alpha(0) + \xi'(0) + (0.5 - a_h)\alpha'(0)]\phi(\tau) + \pi(0.5 + a_h) \\
& \times \int_0^\tau \phi(\tau - \tau_0)[\alpha'(\tau_0) + \xi''(\tau_0) + (0.5 - a_h)\alpha''(\tau_0)]d\tau_0 + \\
& \frac{\pi}{2}a_h(\xi'' - a_h\alpha'') - (0.5 - a_h)\frac{\pi}{2}\alpha' - \frac{\pi}{16}\alpha''. \quad (4)
\end{aligned}$$

171 Here, $\phi(\tau)$ is the Wagner function given by $\phi(\tau) = 1 - 0.165e^{-0.0455\tau} - 0.335e^{-0.3\tau}$. The expression
172 were simplified further and integrated into the equations of motion (see Eqs. 1 and 2) in order to
173 obtain a state-space formulation of first order ordinary differential equations (ODEs). The present
174 study adopts the state-space formulation to calculate the loads at attached flow regime and the
175 details of the same are found out in Lee *et al.*[3]. The initial conditions for pitch, pitch rate, plunge
176 and plunge velocity are chosen as $\alpha(0) = \pi/12$, $\alpha'(0) = 0$, $\xi(0) = 0$ and $\xi'(0) = 0$ in the present
177 study. **Note that this initial condition provides an initial incident angle higher than the**
178 **static stall angle [35].**

179 Modeling of aerodynamic loads under dynamic stall conditions involves accounting for different
180 stages, such as flow separation, vortex shedding, and flow reattachment phases [1], including the
181 loads at the attached flow regime. The variation of load coefficients becomes highly nonlinear
182 in the flow separation and vortex shedding regimes, which need to be accurately modeled either
183 using high fidelity Navier–Stokes solvers [28] or semi-empirical models [35]. Although Navier–Stokes
184 solvers provide an accurate estimation of the aerodynamic loads, they are computationally expensive.
185 Alternatively, semi-empirical models, such as LB model [35] are capable of estimating the loads
186 with an agreeable extent of accuracy while considerably reducing the computation cost. They are
187 widely used in the literature for aeroelastic computations of systems subjected to dynamic stall
188 [10, 12, 14, 15]. Accordingly, the present study uses the LB model to estimate the loads at dynamic
189 stall regimes.

190 The LB model was initially developed in the indicial form [30] using the experimental data
191 of aerodynamic loads at subsonic speed regimes (Mach number (M) < 0.8) and has subsequently
192 been modified into state-space forms [31, 29] for various engineering applications. The LB model
193 uses parameters obtained from static and dynamic stall tests to demarcate the flow regimes and
194 estimate the load coefficients at regular intervals of M values in the subsonic regime. The state-
195 space formulation serves to be advantageous for stability and response analysis as it can be directly
196 coupled with the structural governing equations, and the ODEs in the abridged form are given by
197 [10],

$$x' = f(x, \hat{\alpha}, q), \quad (5)$$

198 where $x = [x_1, x_2, \dots, x_{12}]^T$ are twelve aerodynamic states used to calculate the aerodynamic loads
199 representing the unsteady attached flow, flow separation, vortex shedding, and flow reattachment
200 regimes. q represents the nondimensional effective pitch rate, given by $q = 2\alpha'$ and $\hat{\alpha}$ denotes the
201 effective angle of incidence, given by

$$\hat{\alpha} = \tan^{-1} \left(\frac{\sin \alpha + \xi' \cos \alpha}{\cos \alpha - \xi' \sin \alpha} \right). \quad (6)$$

202 The aerodynamic forces in the LB model are expressed as components perpendicular and parallel to
203 the airfoil chord as it serves to be more convenient in calculations involving rotor blade applications
204 [10]. The coefficients of forces are given as

$$\begin{Bmatrix} C_n \\ C_m \\ C_c \end{Bmatrix} = g(x, \alpha, q), \quad (7)$$

205 where C_c and C_n represent the coefficients of aerodynamic loads with respect to the chord and the
206 normal, respectively. However, the equations of motion require the estimation of lift force (see Eqs.

207 (1) and (2)) which acts perpendicular to the wind flow. In such case, the coefficient of lift (C_l) can
 208 be resolved such that,

$$C_l = C_n \cos \alpha - C_c \sin \alpha. \quad (8)$$

209 The moment and normal force coefficients are estimated using the superposition of loads coefficient
 210 components at each flow module. The LB model is divided into three modules: (i) Unsteady attached
 211 flow module - The load coefficients are calculated using the first eight states ($x_1 - x_8$) which are
 212 modified from Wagner's unsteady formulation by accounting for the compressibility factor of flow,
 213 (ii) Trailing edge separation and reattachment module - the change in load coefficients with respect
 214 to the amount of flow separation calculated using the states x_9 , x_{10} and x_{12} , and (iii) Dynamic
 215 stall or vortex-induced aerodynamic loads - additional loads arising due to the formation of the
 216 vortex on the airfoil surface calculated by state x_{11} . The total loads are given as the summation of
 217 aerodynamic forces from each module by,

$$C_n = C_n^I + C_n^f + C_n^v, \quad C_m = C_m^I + C_m^f + C_m^v, \quad C_c = C_c^f. \quad (9)$$

218 The superscripts, I , f , and v indicate impulsive loads from the attached flow component, trailing
 219 edge separation component, and vortex shedding component, respectively. A detailed description of
 220 the formulation of aerodynamic loads and values of Mach number dependent parameters at regular
 221 intervals of M in the range of 0.3 - 0.8 (the M concerned with the present study ranges from 0.3 -
 222 0.6) can be found in [30, 10, 14] and is not presented here for the sake of brevity. Since the present
 223 study involves accounting for random fluctuations in the flow, giving rise to fluctuations in M as
 224 well, the Mach number dependent empirical parameters inherently become time-varying and need to
 225 be estimated at each time step. Since the empirical parameter values are only known corresponding
 226 to specific M values, at intermediate values of M , a cubic Hermite interpolating polynomial function
 227 is used to estimate the Mach number dependent parameters. The cubic Hermite interpolation
 228 polynomial ensures C^1 continuity which means the fitted curve is continuously differentiable at the
 229 known data points. Finally, aeroelastic equations of motion (Eqs. (1) and (2)) are converted to four
 230 first-order ODEs such that,

$$\begin{Bmatrix} x'_{13} \\ x'_{14} \\ x'_{15} \\ x'_{16} \end{Bmatrix} = \hat{f}(\alpha, \alpha', \xi, \xi', C_l, C_m). \quad (10)$$

231 Here, the state variables x_{13} , x_{14} , x_{15} and x_{16} represent α , α' , ξ and ξ' , respectively - which are
 232 solved using numerical integration.

233 2.3. Karhunen-Loeve Expansion for fluctuating inflow

234 The fluctuations in the longitudinal inflow are generated using the Karhunen-Loeve expansion
 235 (KLE) approach using a prescribed correlation [15, 25]. In KLE, a stochastic process is simulated
 236 as bi-orthogonal decomposition of its correlation function [26]. This essentially means that the on-
 237 coming flow is represented as a random process involving a series expansion of a set of deterministic
 238 functions $u_i(\tau)$ and a vector of independent orthogonal random variables $\eta_i(\theta)$, defined in the prob-
 239 ability space (Ω, ξ, P) and $\theta \in \omega$ (where ω is the sample space). The stochastic inflow velocity is
 240 given by

$$U(\tau, \theta) = U_m + \sum_{i \geq 1} \sqrt{\lambda_i} u_i(\tau) \eta_i(\theta). \quad (11)$$

241 For the ease of representation, dependence on θ is dropped in this paper. The deterministic functions
 242 $u_i(\tau)$ are obtained by solving Fredholm's equation of the second kind [36] given by

$$\int_{\Omega} C(\tau, \tau') \cdot u_i(\tau') d\tau = \lambda_i u_i(\tau), \quad (12)$$

243 where $C(\tau, \tau')$ is the correlation function of $U(\tau)$. Note that $U(\tau)$ is assumed to be a Gaussian
 244 process with a target auto-correlation function

$$R_{UU,tgt}(\tau) = \sigma^2 \cdot e^{-c_1 \tau_{lag}^2}. \quad (13)$$

245 Here, σ^2 is the variance of the process, τ_{lag} is the time lag and c_1 is the correlation coefficient
 246 that governs the fluctuation time scale. The number of terms needed for simulating Eq. 11 is the
 247 minimum "z" satisfying

$$\sum_{i=1}^z \lambda_i \geq 0.99 \sum_{i=1}^n \lambda_i, \quad (14)$$

248 where n is the total number of eigenvalues obtained from the discrete form of Eq. 12.

249 2.4. Time scale of the oncoming flow

250 In field conditions, the oncoming flow comprises different time scales depending upon natural
 251 conditions. While studies in the dynamical systems literature are rife with examples, illustrating
 252 the role played by the time scales of the input noise over the bifurcation characteristics [37], we
 253 specifically focus on the aeroelastic findings presented by Venkatramani *et al.*[25]. For a classical
 254 flutter system, it was shown that based on the correlation length of the input flow and the system
 255 time scale (here, the LCO time period), stochastic input flows could be classified into 'long' and
 256 'short' time scale flow fluctuations. These long or short time scales can individually produce radically
 257 distinct dynamics (at distinct stability regimes). Therefore, an interplay between different time scales
 258 (c_1) and noise intensity (σ) on the aeroelastic dynamics, and in turn the incurred fatigue damage
 259 is investigated in this study. Accordingly, three different types of fluctuating inflows with varying
 260 time-scales are considered in the present study: i) 'Type A' ($c_1 = 0.01$, correlation length ($\tau_{l,A}$)
 261 = 30), ii) 'Type B' ($c_1 = 0.001$, correlation length ($\tau_{l,B}$) = 100) and, iii) 'Type C' ($c_1 = 0.00001$,
 262 correlation length ($\tau_{l,C}$) = 1000). Here, the correlation length is defined as τ_{lag} needed for $R_{UU,tgt}(\tau)$
 263 to approach zero [25].

264 The chosen fluctuating inflows are classified as long time scale or short time scale by comparing
 265 their correlation length with nondimensional system time scale (τ_{sys}) [25], which is found to be 70
 266 in the present system. Hence, 'Type A' inflow is representative of a short time scale (since $\tau_{l,A} <$
 267 τ_{sys}); whereas, 'Type B' and 'Type C' inflows are indicative of long time scales (since $\tau_{l,B}$ and $\tau_{l,C}$
 268 $> \tau_{sys}$). Figures 3(a)-(c) show the variation of flow speed with time simulated for $U_m = 6$ and
 269 $\sigma = 0.3$ and representing fluctuating inflow model 'Type A', 'Type B' and 'Type C', respectively.
 270 The corresponding correlation functions are presented in Figs. 3(d)-(f), respectively. It is observed
 271 that the amplitude of $U(\tau)$ also increases as the correlation length of fluctuating inflow increases.
 272 In the light of the objective of this study to investigate the role of time scales and noise intensity
 273 of the input flow fluctuations on the response dynamics and the corresponding structural safety,
 274 we choose three different noise intensities in the present study. Accordingly, the values of σ are
 275 chosen as 0.1, 0.2 and 0.3. It is worthwhile to mention that a variation in σ is assumed not to
 276 affect the correlation length of fluctuating inflow significantly and therefore elucidating the need for
 277 investigating the effects of time scales and noise intensity of $U(\tau)$ as isolated cases.

278 2.5. Validation of dynamic stall model under stochastic inflow condition

279 The solver's efficacy in estimating the aerodynamic loads in the dynamic stall regime under
 280 fluctuating flow conditions is inspected in the present subsection. This is done by first comparing
 281 the value of C_m calculated using the LB model to the findings from dynamic stall experiments by
 282 McAlister *et al.*[38] under deterministic flow conditions. The comparison of the C_m vs α hysteresis
 283 plot for an airfoil, undergoing forced sinusoidal pitching prescribed as: $\alpha(\tau) = 12 + 10 \sin(\kappa\tau)$, with
 284 the reduced frequency $\kappa = \omega b/V = 0.0976$, obtained from present computation and experiments at
 285 $M = 0.3$ is shown in Fig. 4(a). The hysteresis plot is observed to be in close agreement with the
 286 experimental result substantiating the model's validity in the dynamic stall regime.

287 Next, the present LB model is examined for the fluctuating flow conditions with the same pitch-
 288 ing kinematics. The resulting fluctuations in the M at each time step are incorporated in the model

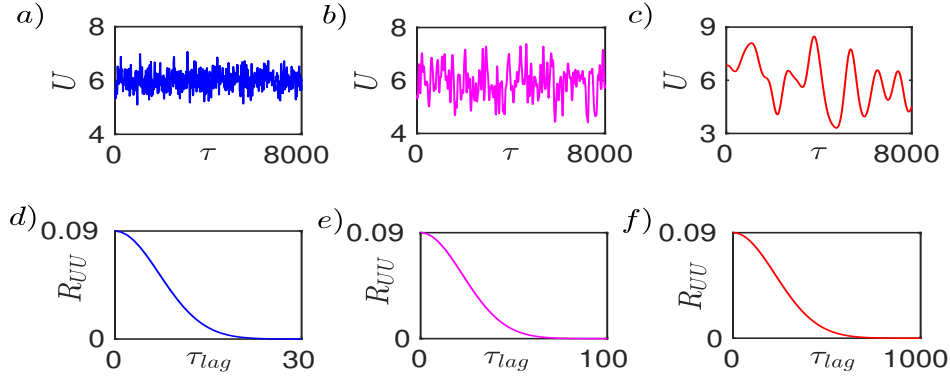


Figure 3: Time history of the fluctuating inflow at $U_m = 6$ for, (a) ‘Type A’ inflow (simulated auto-correlation function depicting the correlation length is shown in (d)), (b) ‘Type B’ inflow (simulated auto-correlation function is shown in (e)), and (c) ‘Type C’ inflow (simulated auto-correlation function is shown in (f)).

289 such that the M value varies from 0.3 to 0.5 as the corresponding Mach number dependent empiri-
 290 cal parameter values are available in the literature [35]. Note that the Mach number dependent
 291 parameters at intermediate values are estimated using the cubic Hermite interpolation technique.
 292 Due to the lack of suitable literature under stochastic inflow to compare, the validity of the solver is
 293 tested by comparing the C_m vs. α hysteresis plot with those obtained for deterministic inflow case
 294 at $M = 0.3, 0.4,$ and 0.5 . The idea behind this is that, if the hysteresis plot for the stochastic case is
 295 in qualitative and quantitative agreement with the individual deterministic cases, the model can be
 296 considered valid for the given conditions. Accordingly, it is observed in Fig. 4(b) that the hysteresis
 297 plot for fluctuating flow case matches qualitatively with the deterministic cases and is observed to
 298 be bounded between the hysteresis plots for $M = 0.3$ and 0.5 cases, respectively. Hence, the present
 299 modeling framework is considered valid even under the stochastic inflow.

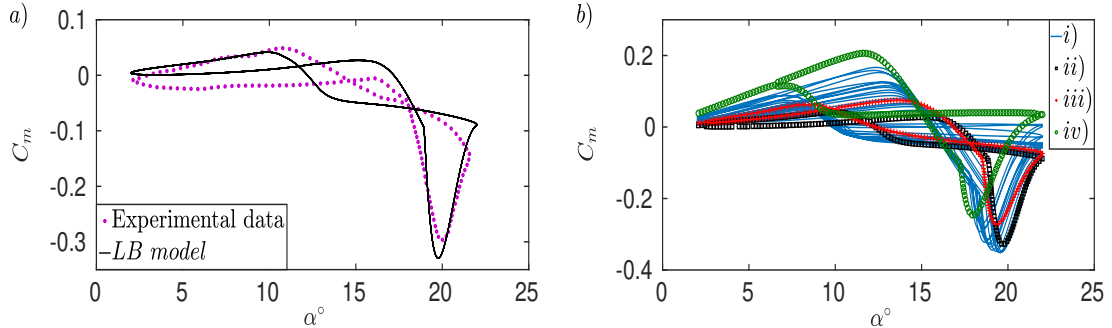


Figure 4: Validation of the LB model in the deterministic and stochastic flow conditions- C_m vs α hysteresis of an airfoil pitching sinusoidally with kinematics : $\alpha(\tau) = 12 + 10 \sin(\kappa\tau)$ at $\kappa = 0.0976$, (a) The efficacy of the LB model is established by comparing the C_m vs α hysteresis curves with experimental data [38] at $M = 0.3$, (b) The hysteresis plots under deterministic flow condition at $M = 0.3, 0.4$ and 0.5 (ii, iii, and iv, respectively) obtained using the LB model, are compared with the hysteresis plot under stochastic flow (i) for mean $M = 0.4$, with the $M(\tau)$ randomly fluctuating between 0.3 - 0.5.

300 2.6. Overview of the rainflow counting algorithm

301 In order to estimate the fatigue damage from the aeroelastic response, RFC is employed in
 302 the present study. The details of this algorithm are briefly presented in this subsection. Under
 303 stochastic input flow conditions, the noise-induced aeroelastic responses give rise to random stress
 304 cycles. Analysis of random stress cycles are done either in frequency domain or in time domain.
 305 Time-domain-based techniques include cycle counting methods such as level crossing, range counting,
 306 and RFC [39]. In the level crossing method, only the peak loads above a set limit are counted, and
 307 others are neglected, while in range counting, the peak and valley of each load cycle are counted to

308 calculate the strength loss after each cycle. However, these approaches result in erroneous fatigue
 309 life predictions in certain cases, particularly where load cycles consist of a combination of low and
 310 high amplitude cycles [39]. RFC, despite not accounting for the sequence of load cycles, is the most
 311 accurate and most widely used method for estimating fatigue damage in most of the engineering
 312 applications [39].

313 The earliest RFC algorithm was developed by Matsuishi and Endo [40] and was named after
 314 the analogy that raindrops are falling from the surface of vertically drawn stress cycles, analogous
 315 to the ‘pagoda roof’. Over the years, different RFC algorithms were developed, and some of them
 316 are listed in [41, 42]. Rychlik[32] gave a new definition of RFC which is illustrated in Fig. 5. This
 317 definition involves finding the largest minima L_k on both sides (t^+ and t^-) of each local maxima
 318 (H_k), between those local maxima (H_k) and the adjacent higher peaks on both sides. Between the
 319 two minima $L_k(t^+)$ and $L_k(t^-)$, the one that corresponds to the minimum downward excursion is
 defined as k^{th} rainflow minima. The RFC amplitude for k^{th} cycle is thus defined as $(H_k - L_k^{RFC})$.

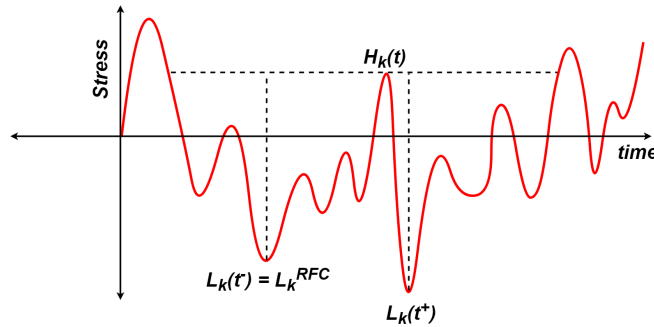


Figure 5: Schematic representation of a typical RFC algorithm [32].

320 To calculate the fatigue damage, a cycle counting rule is typically integrated with a damage
 321 rule. Most widely accepted damage theories are linear accumulation theory given by Palmgren [34],
 322 French’s endurance-based theory [43] and Langer’s two-stage damage based approach [44]. A review
 323 of all the popular fatigue damage methods can be found in Fatemi *et al.*[45]. Although endurance
 324 strength and two-stage-based techniques are much more detailed, the process is computationally
 325 expensive [46]. On the other hand, the linear accumulation theory given by Palmgren is more
 326 popular, particularly for comparative studies of fatigue damage among different models [22, 19], due
 327 to its simplicity and can be combined effectively with the RFC algorithm.

328 Based on Palmgren’s theory, Miner[33] derived a mathematical model called the linear damage
 329 accumulation rule (LDAR) given as $fd = \sum_{n=1}^k (n_i/N_i)$, where n_i is the number of load cycles
 330 corresponding to i^{th} load level, N_i is the number of load cycles to fail at that level and k is total
 331 number of load levels. LDAR is a robust methodology for estimating the fatigue damage based on
 332 the assumption of constant energy absorption associated with each cycle [45]. If the net fatigue
 333 damage value (fd) approaches unity, it implies that the structure has failed.
 334

335 3. Numerical aeroelastic response analysis

336 The present study aims to investigate the dynamical characteristics of a canonical pitch-plunge
 337 aeroelastic system subjected to deterministic and stochastic inflows. The response dynamics is
 338 compared among linear and nonlinear structural stiffness cases under attached flow (linear) and
 339 dynamic stall (nonlinear) conditions. Next, the stresses developed in the structure due to aeroelastic
 340 oscillations and the resulting fatigue damage accumulated in the structure are estimated. This
 341 section deals with the analysis of the response dynamics of the system. To that end, the state-
 342 space form of the coupled governing equations in terms of first-order ODEs are solved using the
 343 fourth-order Runge-Kutta numerical integration technique with increasing mean flow speed. An
 344 adaptive time-stepping with a tolerance (both absolute and relative) of $\mathcal{O}(10^{-6})$ is used for the
 345 deterministic inflow case. On the other hand, a fixed time step of 10^{-4} is chosen through a time
 346 step independence test to acquire the numerical solutions for the stochastic inflow case, ensuring the

347 stability of the numerical integration scheme. The nondimensional structural parameters are chosen
 348 from Lee *et al.*[3] and are given in Table 1. To incorporate the structural nonlinearity, a cubic
 349 nonlinear stiffness in the pitch DoF with $\beta_\alpha = 5$ is chosen for this study. Each case for deterministic
 350 or stochastic inflow under attached flow and dynamic stall regimes is simulated for $\tau = 0-8000$, and
 351 the time responses are presented in the following subsections. Note that the average simulation time
 352 for each deterministic case under isolated structural nonlinearity is approximately 30s, and under
 353 aerodynamic/coupled structural-aerodynamic nonlinearity is approximately 3000s. For solutions of
 354 each stochastic case under pure structural nonlinearity, computation time is approximately 1500s,
 355 and for pure aerodynamic nonlinearity and combined structural/aerodynamic nonlinearity, it is
 356 approximately 36000s. The present simulations are performed on a workstation configured with an
 357 Intel® Core™ i7-9700 CPU @ 3.00GHz - 8 processors and 64 GB RAM.

Table 1: The nondimensional structural parameters of the aeroelastic system [3].

μ	r_α	x_α	a_h	ϖ
100	0.5	0.25	-0.5	0.2

358 3.1. Structural responses under deterministic flow conditions

359 This subsection focuses on investigating the system response under deterministic flow scenarios.
 360 First, the sole effects of isolated structural and aerodynamic nonlinearities on the responses signa-
 361 tures are studied. To that end, the structure is considered to possess a cubic nonlinear stiffness
 362 in pitch DoF under attached (linear) flow conditions. The unsteady linear formulation based on
 363 Wagner’s function is used to model the aerodynamic loads in this regime. The bifurcation plot with
 364 U as the control parameter is shown in Fig. 6(a). It is observed that the system response transitions
 365 from a fixed point to LCO response at $U = 6.25$, beyond which the amplitude of LCOs increases
 366 gradually, characterized by the occurrence of a super-critical Hopf bifurcation [3].

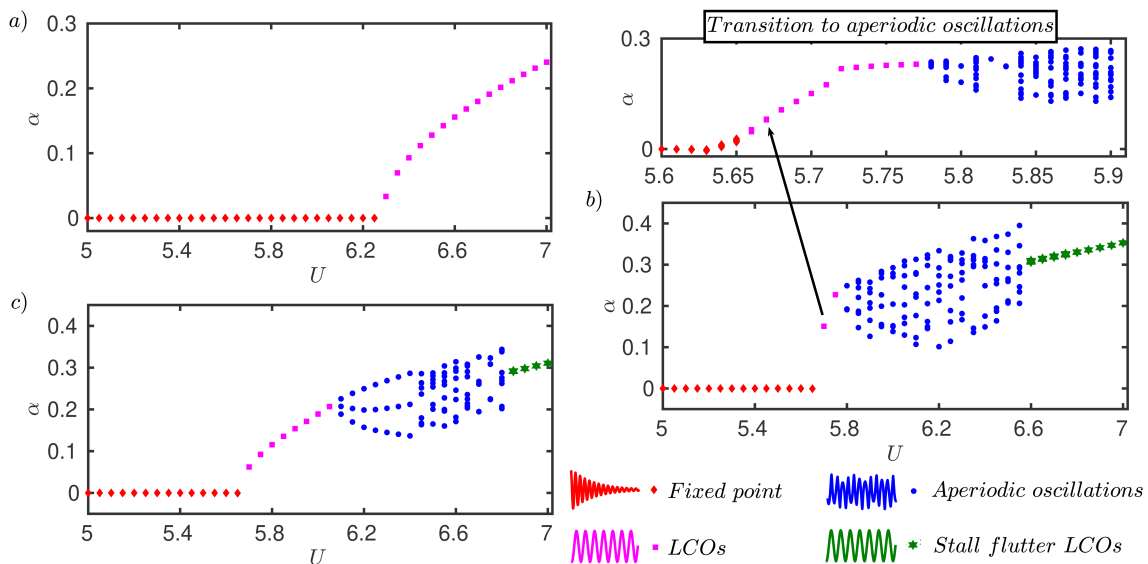


Figure 6: Bifurcation diagrams of pitch response considering the flow speed as the control parameter for (a) nonlinear structure and linear aerodynamics, (b) linear structure and nonlinear aerodynamics, and (c) both nonlinear structure and aerodynamics.

367 Next, the response dynamics of a linear structure (*i.e.*, $\beta_\alpha = 0$ in Eq. 2), subjected to dynamic
 368 stall conditions are studied using the LB model to investigate the isolated effects of aerodynamic

369 nonlinearity. It is observed in Fig. 6(b) that the onset of LCOs occurs at $U = 5.65$, which then
370 transition into aperiodic responses at $U = 5.8$. A zoomed view of the responses between $U = 5.6$ - 5.9
371 is also presented in Fig. 6(b), showing the transition from fixed point to aperiodic oscillations via an
372 LCO regime. The onset of aperiodicity marks the first occurrence of a dynamic stall event, which
373 is evident from the $x_9 - x_{10}$ and $\alpha - \alpha'$ phase plots (see Fig. 7). Dynamic stall phenomenon in LB
374 model is characterized by the discontinuous boundaries present at $x_9 = \pm C_{n1}$ (onset of stall/ flow
375 reattachment) and $x_{10} = 0.7$ (dynamic trailing edge separation point corresponding to static stall
376 angle). Note that x_9 and x_{10} represent the state values of the LB model and details of the same can
377 be found in our recent work [14]. Fig. 7(a) shows that the flow remains attached at $U = 5.66$, as
378 the x_9 and x_{10} values do not cross the discontinuity boundaries. At $U = 5.79$, value of x_9 crosses
379 $\pm C_{n1}$ and x_{10} approaches 0.3, indicating that the trailing edge separation point lies at $0.3c$ from the
380 leading edge and the response dynamics switches aperiodically between deep and light dynamic stall
381 events (Fig. 7(b)). Note that light stall regime corresponds to amplitude of oscillations reaching
382 static stall angle-of-attack which lies closely to the AoA at $x_{10} = 0.7$ and deep stall regimes lie
383 beyond light stall regimes, where a large vortex spends significant time on the airfoil surface before
384 shedding. The aperiodic nature of the responses at $U = 5.79$ is further substantiated by the $\alpha - \alpha'$
385 phase portrait shown in Fig. 7(e). As U reaches 6.6, $x_9 - x_{10}$ phase portrait (see Fig. 7(c)) shows that
386 the dynamics enter into deep stall event completely and the response signature becomes periodic,
387 marking the onset of stall flutter LCOs (see Fig. 7(f)).

388 Next, the combined effect of structural cubic hardening nonlinearity and aerodynamic nonlin-
389 earity governed by dynamic stall on the system responses is investigated. The bifurcation plot for
390 the same is provided in Fig. 6(c). It is observed that the onset of flutter instability occurs almost at
391 the same flow speed ($U = 5.65$) as in the case of isolated aerodynamic nonlinearity (see Fig. 6(b)).
392 It is worth noting that the bifurcation point has shifted to lower flow speed as compared to the
393 system with isolated structural nonlinearity. This may be attributed to the LB model's capability of
394 accounting for the nonlinear effects from the flow (wake effects from flow separation and accounting
395 for compressibility). Therefore, it is conjectured that the presence of nonlinearities in flow advances
396 the bifurcation onset in the response signatures. Furthermore, the LCOs occurring post-bifurcation
397 span over a larger flow speed regime, and the transition to aperiodic responses (at $U = 6.45$) from
398 LCOs occurs via a short regime of period-3 oscillations between $U = 6.1$ - 6.4 . The onset of large-
399 amplitude stall flutter LCOs is observed to be postponed to $U = 6.8$ as compared to $U = 6.6$ in the
400 case of a system with isolated aerodynamic nonlinearity (see Fig. 6(b)).

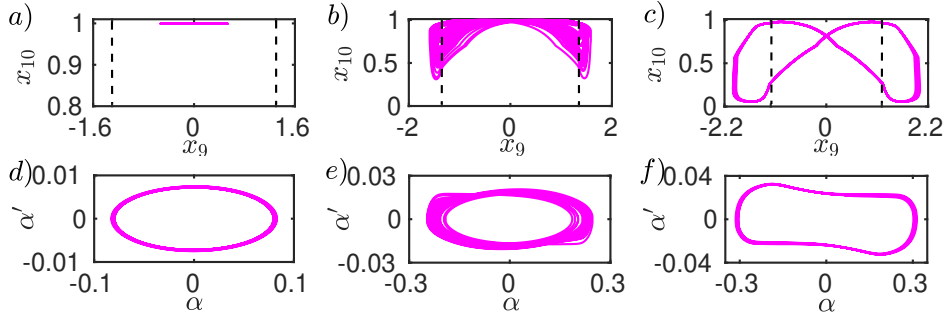


Figure 7: $x_9 - x_{10}$ phase portrait (a) at $U = 5.66$, corresponding to the onset of LCOs, (b) at $U = 5.79$, showing the transition of LCOs to aperiodic oscillations and (c) at $U = 6.6$, corresponding to the stall flutter oscillations. The dashed lines in (a-c) indicate $\pm C_{n1}$. The $\alpha - \alpha'$ phase portrait of the response signatures at (d) $U = 5.66$, (e) $U = 5.79$ and (f) $U = 6.6$.

401 So far, the bifurcation scenarios in the deterministic aeroelastic system with isolated nonlinearity
402 either in the structure or flow, followed by combined nonlinearities are presented. Equipped with
403 this insight, we repeat this exercise for the nonlinear aeroelastic system subjected to randomly
404 fluctuating input wind in the next subsection.

405 3.2. Structural responses under stochastic flow conditions

406 In this part, the time responses of the system with isolated nonlinearity in structure and flow
407 are obtained first, followed by an investigation into the effect of coupled nonlinearities on system

408 responses under stochastic flow conditions achieved by randomly varying the inlet velocity about
409 a mean value of (U_m). It is worthwhile to mention that bifurcation diagrams cannot be explicitly
410 presented in the stochastic case - as found in Fig. 6. Indeed, one needs to invoke the concepts of
411 stochastic bifurcations via the evolution of probability density function, and/or estimate Lyapunov
412 exponents, and/or estimate Shannon entropy as elaborated in Venkatramani *et al.* [26]. Doing the
413 same is beyond the scope of objectives entailing in the present study. Therefore, we restrict our
414 discussions by merely presenting the time histories of the responses and use visual inspection to
415 discern the qualitative nature of the stochastic aeroelastic responses (in lines with [25]). Recalling
416 the discussions in Sec. 2.4, three different types of fluctuating inflow, involving different time scales -
417 defined as ‘*Type A*’, ‘*Type B*’ and ‘*Type C*’ are considered in this study with various noise intensities
418 ranging from 0.1 to 0.3. It is to be noted that only selected cases representative of notable transitions
419 impacting structural safety are discussed in this paper for the sake of brevity.

420 Fluctuating inflow imposed upon structure possessing pitch cubic hardening nonlinearity under
421 attached flow condition is observed to significantly alter the response dynamics of the system (see
422 Fig. 8) and is consistent with the observations reported hitherto [47, 26]. The time scale of the
423 flow, on the other hand, is observed to play a major role in defining the qualitative nature of the
424 response characteristics. Therefore, as a starting step, a larger emphasis is placed on demarcating
425 the response dynamics at different time scales at a constant value of $\sigma = 0.3$. Subsequently, the
426 effect of different σ values on the system response is investigated in this study and is presented in
427 the later part of this subsection.

428 Under ‘*Type A*’ inflow (corresponding to a short time scale), the pitch response at $U_m = 5.6$
429 decays to a fixed point (see Fig. 8(a)) and at $U_m = 6$, a transient “burst” of oscillations appear
430 which then switch to a fixed point signature; see Fig. 8(b). At $U_m = 6.6$, large-amplitude LCOs
431 with random variations in the amplitude are observed; see Fig. 8(c). Finally at $U_m = 7$, response
432 transitions to well developed random LCOs; see Fig. 8(d). Note that the intermittency route to
433 random LCOs presented here are consistent with the observations of Venkatramani *et al.* [25, 26, 27].

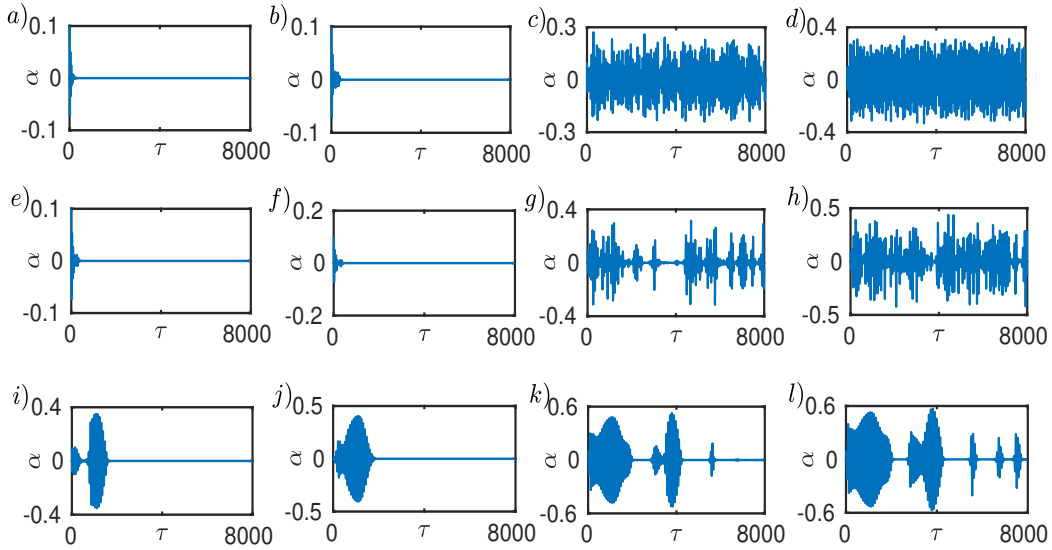


Figure 8: Pitch responses of system possessing structural nonlinearity under attached flow conditions subjected to stochastic inflow conditions with $\sigma = 0.3$; for ‘*Type A*’ inflow at (a) $U_m = 5.6$, (b) $U_m = 6$, (c) $U_m = 6.6$, and (d) $U_m = 7$; for ‘*Type B*’ inflow at (e) $U_m = 5.6$, (f) $U_m = 6$, (g) $U_m = 6.6$, and (h) $U_m = 7$; and for ‘*Type C*’ flow at (i) $U_m = 5.6$, (j) $U_m = 6$, (k) $U_m = 6.6$, and (l) $U_m = 7$. The pitch angle presented throughout the manuscript are in radians.

434 Under ‘*Type B*’ fluctuating inflow, involving a time scale slightly larger than the system time
435 scale, the system responses at $U_m = 5$ and $U_m = 6$ are seen to be similar to those observed for the
436 ‘*Type A*’ inflow (see Fig. 8(e) and Fig. 8(f)). However, as U_m is increased, the time responses are ob-
437 served to possess sporadic bursts of periodic oscillations switching intermittently with low amplitude

438 oscillations or rest/off regimes (see Fig. 8(g) and Fig. 8(h)). This is indicative of “burst-type” inter-
439 mittency [25]. It is to be cautioned that ‘*Type B*’ input flow possesses a time scale only marginally
440 higher than the system time scale and can be perhaps defined as input flows with “moderate” time
441 scales. Venkatramani *et al.* [25] on the other hand, used isolated cases of extremely short time scale
442 input flows (wherein the correlation time of the random input wind is very short compared to the
443 system time scale) and reported regimes of intermittent periodic oscillations amidst low-amplitude
444 aperiodic oscillations - which was termed to be “burst” type intermittency in aeroelastic responses.
445 One needs to be mindful of the distinct correlation structure found in the ‘*Type B*’ fluctuating
446 inflow and thereby in interpreting the responses presented in Figs. 8(g) and 8(h) as “burst” type
447 intermittency. Studies on the correlation structure of the random input process, hand-in-hand with
448 the noise characteristics [48] have shown that the genre of noise-induced intermittency in dynamical
449 systems needs closer attention in attributing terminologies. Nevertheless, given that the present
450 work is focused on utilizing the stochastic aeroelastic responses to compute the fatigue damage,
451 carrying out investigations into the genres of noise-induced intermittent aeroelastic responses will
452 be beyond this study.

453 Under ‘*Type C*’ flows (see Figs. 8(i) - 8(l)), involving a long time scale, one observes sporadic
454 periodic oscillations at lower values of U_m , which eventually gives away to a decaying signature. As
455 U_m increases, periodic oscillations (“on” state) are found interspersed amidst segments of decaying
456 signatures (“off” state), and thereby called noise-induced “on-off” intermittency. The time responses
457 presented in Fig. 8 are consistent with the findings presented in [47, 25, 27]. It is worth noting that
458 the responses presented in Fig. 8 for flows characterized as ‘*Type B*’ and ‘*Type C*’ transition to
459 random LCOs for larger values of U_m . However, for reasons described in the next part involving
460 dynamic stall, we refrained from showing the eventual culmination of intermittent responses into
461 random LCOs.

462 Next, we turn our attention to the response dynamics of the system with only aerodynamic
463 nonlinearity under randomly fluctuating flow conditions with different time scales. In this case,
464 the amplitude of the pitch response is much higher than those obtained for isolated structural
465 nonlinearity. The qualitative nature of the pitch responses here as well shows different intermittent
466 signatures under different time scales. For the ‘*Type A*’ inflow, one observes a fixed point response
467 for low values of U_m that transforms itself into fully developed LCOs at higher values of U_m ; see
468 Figs. 9(a)-(d). Though “burst” type intermittency is observed at intermediate values of U_m , we
469 have refrained from explicitly presenting them here to maintain consistency in the U_m values used
470 throughout this manuscript. The “burst” type intermittency route to fully developed LCOs are
471 shown for the ‘*Type B*’ inflow; see Figs. 9(e)-(h). In accordance with using a long time scale input
472 flow, ‘on-off’ intermittent behavior is observed under ‘*Type C*’ inflow for $U_m = 6-7$ (see Fig. 9(j),
473 Fig. 9(k) and Fig. 9(l)). The amplitude of the ‘on’ states increases gradually with the mean flow speed
474 and eventually transforms into LCOs. Note that though the LCOs are observed in higher values
475 of U_m , we have refrained from presenting them here. This is so because the aerodynamic forces
476 modeled via the LB formulation are *acceptable* and *accurate* for restrictive values of α [31, 1, 13].
477 Indeed, the availability of experimental parameters needed for the LB model is usually well available
478 for $\alpha < 40^\circ$ (≈ 0.7 radians) [13]. Therefore, though in line with the hitherto studies [25, 14], an
479 intermittency route to LCO is encountered in the present case, the accuracy of the responses once
480 $\alpha > 40^\circ$ becomes a concern. In turn, we avoid presenting the responses obtained at higher values
481 of U_m . Given the need to compare the time histories of the responses, and correspondingly, the
482 accumulated fatigue damage; the LCOs obtained even from unsteady aerodynamic formulations at
483 higher values of U_m are not presented earlier in Fig. 8.

484 Next, the time responses corresponding to the system possessing both structural and aerodynamic
485 nonlinearities (coupled nonlinearities) are obtained and shown in Fig. 10. From visual inspection,
486 it is evident that the aeroelastic responses obtained from the system with coupled nonlinearities
487 are qualitatively similar to the responses of a system with a linear structure subjected to nonlinear
488 aerodynamic loads (see Fig. 9). The responses are also found to be consistent with the findings from
489 [14]. However, the amplitude of responses is observed to be reduced with the inclusion of a cubic
490 hardening nonlinearity in the structural stiffness behavior, as compared to the system responses
491 under pure aerodynamic nonlinearity reported in Fig. 9.

492 It is worth reiterating that the presented aeroelastic dynamics are stochastic and nonlinear.

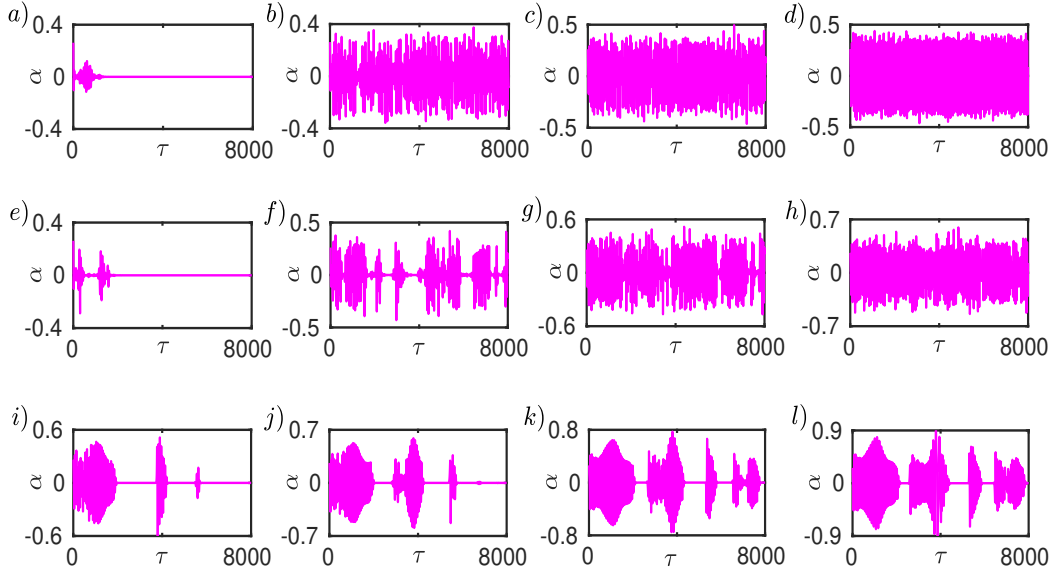


Figure 9: Pitch responses of system with linear structure under nonlinear flow conditions subjected to stochastic inflow conditions with $\sigma = 0.3$; for ‘Type A’ inflow at (a) $U_m = 5.6$, (b) $U_m = 6$, (c) $U_m = 6.6$, and (d) $U_m = 7$; for ‘Type B’ inflow at (e) $U_m = 5.6$, (f) $U_m = 6$, (g) $U_m = 6.6$, and (h) $U_m = 7$; and for ‘Type C’ inflow at (i) $U_m = 5.6$, (j) $U_m = 6$, (k) $U_m = 6.6$, and (l) $U_m = 7$.

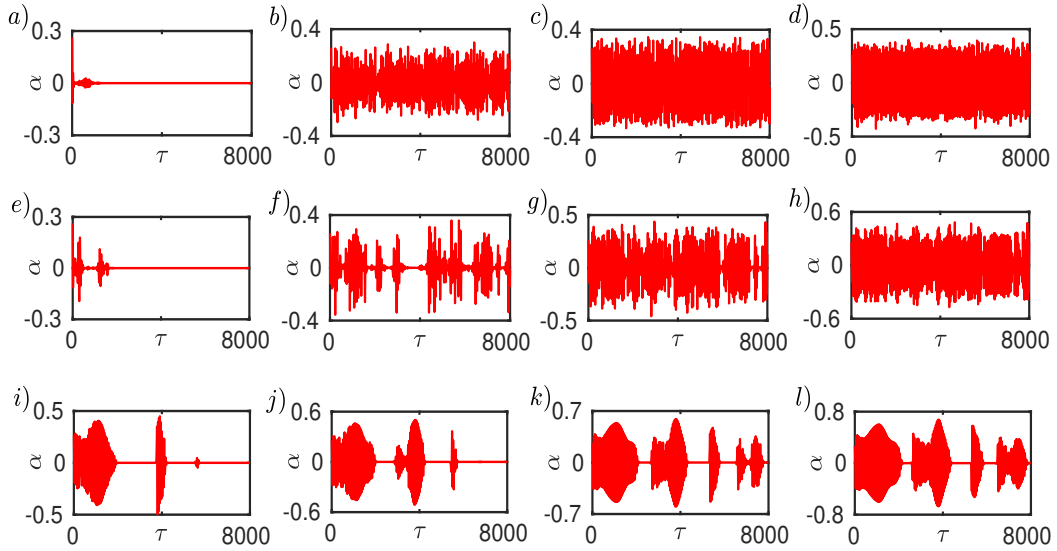


Figure 10: Pitch responses of system with nonlinear structural stiffness behavior under nonlinear flow conditions subjected to stochastic inflow conditions with $\sigma = 0.3$; for ‘Type A’ inflow at (a) $U_m = 5.6$, (b) $U_m = 6$, (c) $U_m = 6.6$, and (d) $U_m = 7$; for ‘Type B’ inflow at (e) $U_m = 5.6$, (f) $U_m = 6$, (g) $U_m = 6.6$, and (h) $U_m = 7$; and for ‘Type C’ inflow at (i) $U_m = 5.6$, (j) $U_m = 6$, (k) $U_m = 6.6$, and (l) $U_m = 7$.

493 In other words, the qualitative and quantitative characteristics are dictated by the genres of the
 494 nonlinearity (type, location, and strength of the nonlinearity) and genres of the random input flow
 495 (noise intensity, time scales, and probabilistic distributions). Given the goal of this work to hand-
 496 in-hand characterize the incurred fatigue damage against the dynamical signature, a brief attempt
 497 to characterize the time responses by varying the noise intensity of ‘*Type A*’, ‘*Type B*’ and ‘*Type*
 498 *C*’ inflow fluctuations are presented next. It is to be cautioned to the reader that though ‘*Type*
 499 *A - Type C*’ inflow have different time scales, a change in the noise intensity can affect the time
 500 scale of the random process as well [25, 26]. Disregarding the interdependence of the time scale
 501 and noise intensity of the random process, for the ease of mathematical modeling, we present the
 502 aeroelastic response dynamics by merely varying the noise intensity σ and assume that this exercise
 503 has no considerable impact on the time scales of ‘*Type A - Type C*’ inflow. Another important
 504 probabilistic marker that can considerably affect the signature of the aeroelastic responses, and
 505 in turn, the structural safety/fatigue damage accumulation, is the probability distribution of the
 506 input random wind. Recall that in Eq. 12, $U(\tau)$ is assumed to be a Gaussian random process.
 507 Introduction of non-Gaussian distributions and investigating the aeroelastic dynamics along with
 508 the fatigue analysis are rife with computational challenges and would demand a separate study.

509 Accordingly, fixing $U_m = 6.6$, we present three cases of noise intensity (namely, $\sigma = 0.1, 0.2$ and
 510 0.3) for the flows represented via ‘*Type A - Type C*’; see Fig. 11. For the ‘*Type A*’ inflow case,
 511 representing the short time flow fluctuations, one observes that an increase in the noise intensity
 512 augments the random variations in the peak amplitudes of the LCOs and is akin to that reported in
 513 [26]. In the ‘*Type B*’ case, an increase in the noise intensity transforms the sustained LCOs into a
 514 “burst” type intermittency, albeit with minimal presence of the aperiodic oscillations. As elaborated
 515 in Krishna *et al.* [48], without a hand-in-hand analytical knowledge of the noise intensity, time
 516 scale, and the probabilistic distributions, it would be premature to comment on the genre of the
 517 intermittency as well as the extent of *laminarity length* (which dictates the duration of aperiodic
 518 fluctuations). Interestingly, increasing the noise intensity to 0.3 transforms the response dynamics
 519 into a visibly evident “burst” intermittency - indicating a delayed onset of LCOs [26] - which in
 520 turn can affect the accumulated fatigue damage. This will be taken up in the next part. For the
 521 ‘*Type C*’ flow case, corresponding to long time scale flow fluctuations, it is observed that despite
 522 an increase in the noise intensity from 0.1 to 0.3 , the “on-off” type intermittency is consistently
 523 observed; albeit with varying laminarity length. Random LCOs are not captured, perhaps due to
 524 a considerable shift in its onset [25]. Indeed, the appearance of “on-off” type intermittency and its
 525 culmination into sustained LCOs depends on the flow speed remaining above or below the critical
 526 limit for a sufficient duration of time; refer to Venkatramani *et al.* [25] for detailed discussions on
 527 the same for a stochastic classical flutter system.

528 To demonstrate the same for the present aeroelastic system, we show the variations of $U(\tau)$ versus
 529 τ for the ‘*Type C*’ flow in Fig. 12. At lower intensity of fluctuations, $U(\tau)$ fluctuates continuously
 530 above the critical flow speed U_{cr} (see Fig. 12(a)). Consequently, the corresponding aeroelastic
 531 response is a sustained LCO; see Fig. 12(d). Increasing σ , $U(\tau)$ fluctuates above and below U_m (see
 532 Fig. 12(b)) and correspondingly giving rise to “on-off” type intermittency in the aeroelastic response;
 533 see Fig. 12(e). This trend is observed even when the noise intensity becomes 0.3 (see Fig. 12(c)).
 534 However, the extent of time it stays above and below the critical speed is different owing to the
 535 changed noise intensity. As discussed earlier, the time scale and intensity of fluctuations dictate this
 536 mapping between the randomness in the input flow and the noise-induced “on-off” intermittency in
 537 the output dynamics [48].

538 So far, it is observed that nonlinearity arising from structure and flow has different effects on
 539 system dynamics under deterministic conditions. Structural nonlinearity restricts the divergent
 540 oscillations to LCOs beyond the critical flutter boundary under the assumption of the attached wake.
 541 Under aerodynamic nonlinearity, structure manifests phenomenologically richer dynamic responses
 542 governed by flow separation and reattachment. On the other hand, time scales and noise intensity
 543 of the fluctuating inflow are crucial in determining aeroelastic responses under stochastic conditions.
 544 At this interim juncture we note the following.

- 545 • Based on the time-scales of the input flow fluctuations, one can either encounter “on-off” type
 546 or “burst” type intermittent behavior.

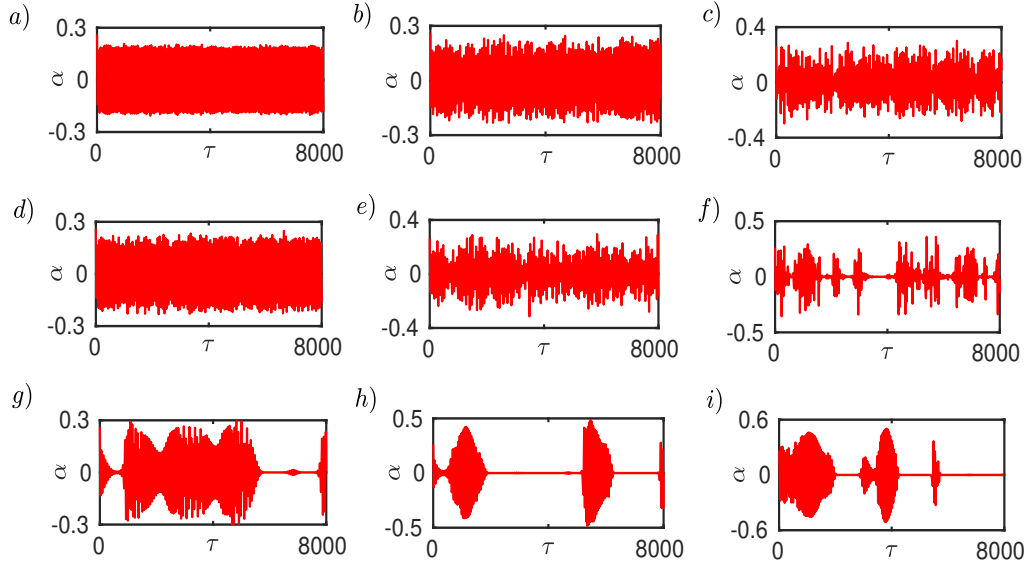


Figure 11: Effect of intensity of fluctuating inflow on aeroelastic responses at $U_m = 6$ under nonlinear aerodynamic loads and nonlinear structure; time histories with 'Type A' inflow for, (a) $\sigma = 0.1$, (b) $\sigma = 0.2$, and (c) $\sigma = 0.3$; time histories with 'Type B' inflow for, (d) $\sigma = 0.1$, (e) $\sigma = 0.2$, and (f) $\sigma = 0.3$; time histories with 'Type C' inflow for, (g) $\sigma = 0.1$, (h) $\sigma = 0.2$, and (i) $\sigma = 0.3$.

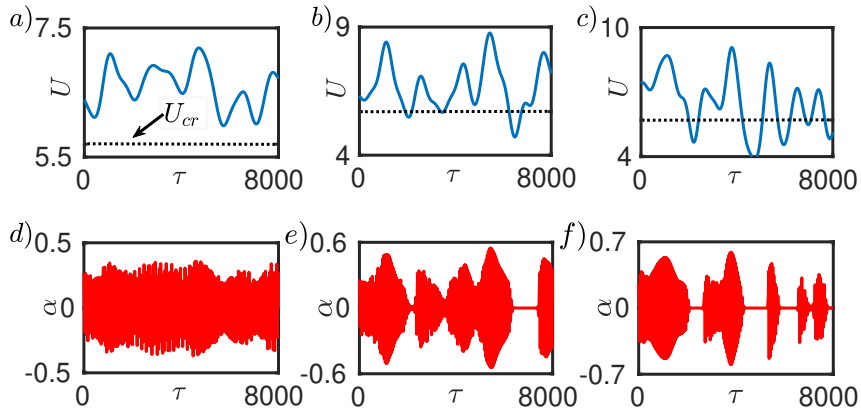


Figure 12: Effect of intensity of fluctuating inflow on aeroelastic responses at $U_m = 6.6$ for 'Type C' inflow under nonlinear aerodynamic loads and nonlinear structure. Time histories of 'Type C' inflow at $U_m = 6.6$ for, (a) $\sigma = 0.1$, (b) $\sigma = 0.2$, and (c) $\sigma = 0.3$; and corresponding pitch responses for (d) $\sigma = 0.1$, (e) $\sigma = 0.2$, and (f) $\sigma = 0.3$, respectively. The critical flutter velocity (U_{cr}) is 5.65 and shown by dashed lines.

- 547 • If the input wind fluctuates with predominantly long time scales, the aeroelastic dynamics
548 switches between high-amplitude periodic oscillations called “on” states, and states of de-
549 cayed oscillations called “off” states. A hand-in-hand increase in noise intensity of the flow
550 fluctuations result in increased switching between the “on” and “off” states.
- 551 • If the input wind fluctuates with predominantly short time scales, the dynamics of the airfoil
552 displays near random switching between states of periodic oscillations interspersed amidst
553 states of aperiodic oscillations. As observed in [26], an increase in fluctuation intensity yields
554 in an easier hopping of trajectories from one attractor to another, leading to unpredictable
555 stitching’s in the intermittent dynamics. In otherwise, the average laminarity length of the
556 noise-induced intermittency in our considered stall flutter system gets altered [48].

557 It is worth reiterating that though few studies on stochastic stall flutter systems exist hitherto [22,
558 15, 14], minimal attempts have been made to characterize the noise-induced transitions in the route
559 to stochastic stall flutter. Consequently, the impact of probabilistic markers like time scales of the
560 input fluctuating flow, and its noise intensities over the nature of the response dynamics has remained
561 largely unexplored. The present study makes its first end of contribution by presenting the noise-
562 induced intermittency as an intermediate stage of oscillations that can ultimately culminate into
563 torsionally dominant random LCOs (stochastic stall flutter). Indeed, one observes that numerous
564 studies on engineering that encountered noise-induced intermittency have taken elaborate steps to
565 develop measures that can predict both (i) transitions to intermittency from state of low amplitude
566 oscillations [49, 50, 51] and (ii) transitions from intermittency to large amplitude LCOs [52, 53],
567 underscoring the need for structural safety assessment. For the considered stochastic stall problem,
568 we address this end of specific concern in the next section. For the sake of comparison, we compare
569 the fatigue damages incurred in classical flutter systems as found in [19].

570 4. Fatigue damage analysis

571 Complex dynamical signatures in stochastic nonlinear aeroelastic systems can presumably induce
572 a considerable amount of fatigue damage in the aeroelastic structures. Indeed, one can conjecture
573 that repeating time histories (of different patterns) can give rise to complex stress cycle reversal
574 and fatigue damage to the aeroelastic system. Unlike the failure that occurs through the first
575 passage of time, fatigue damage accumulation is usually not noticed until the appearance of fatigue
576 cracks, which can rapidly propagate towards a fracture failure. Noting that the development of
577 fatigue failure can be more rampant in the vicinity of LCOs, Venkatramani *et al.* [26] developed
578 a suite of measures that can foretell an impending flutter in a stochastic aeroelastic system with
579 cubic stiffness nonlinearity, and thereby changing the operating conditions to dissuade the onset
580 of this instability. The present study deals with far more complex nonlinearities and fluctuating
581 flow parameters, thereby giving rise to various dynamics and random LCOs. The accumulation of
582 fatigue damage in these corresponding response dynamics and the augmenting role of nonlinearities
583 and randomness in the input flow remains undocumented in the hitherto literature. Addressing this
584 issue is a focal objective of this study, and the methodology to do the same are elucidated next.

585 The aeroelastic system is assumed to be a cantilever beam of 20 m length and uniform cross-
586 section. Although the loading on wings and blades under fluid-structure interaction is complex, a
587 uniformly distributed loading is considered here. The cross-section is taken as a NACA 0012 airfoil
588 with a cord length of 0.61 m. Here, only pitch-plunge responses obtained for a 2-DoF reduced-order
589 model are used to obtain stresses in a 3D aeroelastic structure- akin to that in Venkatesh *et al.* [19].

590 The airfoil is subjected to multi-axial loading, bending stress due to plunging motion, and tor-
591 sional stress due to pitching motion. To convert the state of stress from multi-axial to uniaxial, signed
592 von Mises criteria given by Bracessi *et al.*[54] is implemented. Signed von Mises criterion possesses
593 sudden jumps associated with stress reversal, and yet owing to its ease of computing the damage
594 accumulation - one resorts to using this criterion. The airfoil material is assumed to be isotropic,
595 composed of aluminum alloy *Al 6082-T6*, having modulus of elasticity (E) = 70 GPa, shear modulus
596 (G) = 26.4 GPa and yield strength 250 MPa and is same as that provided in [19]. Under reversible
597 loading, $S - N$ characteristics or stress amplitude (S) vs number of cycles to failure (N) relationship
598 for *Al 6082-T6* are experimentally obtained by Carpinteri *et al.* [55]. Under reversible bending

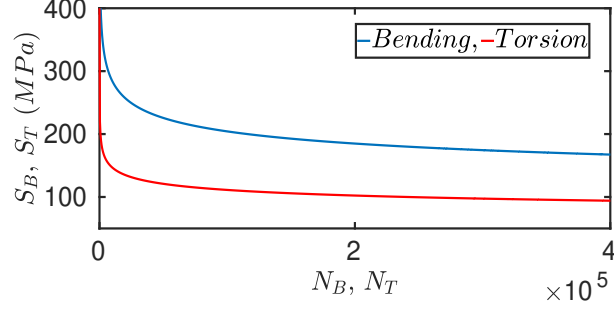


Figure 13: S-N curves for the material for bending and torsional stress.

stresses, $S_B = 1067 \times N_B^{0.1436}$ and under reversible torsional stresses, $S_T = 446.3 \times N_T^{0.1207}$, where S_B and S_T are reversible bending and torsional stress amplitudes, respectively, and N_B and N_T are the number of cycles to fail under S_B and S_T , respectively.

Due to plunge motions, normal bending stresses will be developed, proportional to the displacement (y) of the section above the neutral axis. Additionally, there will be a net shear force and hence shear stress in the y -direction. However, the magnitude of the shear stresses due to bending is observed to be inconsiderable as compared to normal bending stresses, which is also shown in [19]. Hence, only normal bending stresses are taken into consideration here. From the theory of simple bending, bending stress is given as $\sigma_{zz} = (M_b/I)y$, where M_b is the bending moment, and I is the area moment of inertia of the airfoil cross-section about the x -axis. The stresses will be highest at the maximum thickness or y_{max} .

Calculation of torsional stresses due to pitching motion is rather complicated to evaluate as warping is a significant factor due to non-circular cross-section. Due to warping, there will be out of plane displacement also (i.e., in the z -direction), which will be proportional to the rate of twist θ and a function $\psi(x, y)$, such that $\Delta z = \theta\psi(x, y)$. The product $z\theta$ is the rotation of the cross section at z distance and is obtained from pitch time histories. All direct strains and shear strain in x - y plane are zero and hence corresponding stresses are also zero. Remaining two shear strains (γ_{zx}) and (γ_{zy}) are given as [19],

$$\gamma_{zx} = \theta \left(\frac{\partial \psi}{\partial x} - y \right), \quad \gamma_{zy} = \theta \left(\frac{\partial \psi}{\partial y} + x \right). \quad (15)$$

The corresponding shear stresses are given as $\sigma_{zx} = G\gamma_{zx}$ and $\sigma_{zy} = G\gamma_{zy}$. Consequently,

$$\frac{\partial \sigma_{zy}}{\partial x} - \frac{\partial \sigma_{zx}}{\partial y} = 2G\theta. \quad (16)$$

A stress function called Prandtl stress function (ϕ) is now introduced such that, $\sigma_{zx} = \partial\phi/\partial y$ and $\sigma_{zy} = -\partial\phi/\partial x$. Substituting (ϕ) into Eq. 16, we obtain

$$\frac{\partial^2 \phi}{\partial y^2} + \frac{\partial^2 \phi}{\partial x^2} = -2G\theta. \quad (17)$$

For a symmetric airfoil such as NACA 0012, the cross section is given as, $y = a\zeta(x/c)$ and $y = -a_1\zeta(x/c)$, where $\zeta(x/c) = (x/c)^{m_1} [1 - (x/c)^{p_1}]^{q_1}$. The value of stress function ϕ for a symmetric airfoil section is given as

$$\phi = A(y - a\zeta)(y + a_1\zeta), \quad (18)$$

where $A = -G\theta/[1 + (\alpha_1/c^2)(a^2 + a_1^2 + aa_1)]$ and the parameters a , a_1 , p_1 , q_1 , m_1 and α_1 are constants for a particular airfoil cross section. For a NACA 0012 airfoil section, the parameters are obtained as $a = 0.94$, $a_1 = 0.94$, $p_1 = 0.139$, $q_1 = 1$, $m_1 = 0.75$, $\alpha_1 = 0.0083$. More details of stress calculations and NACA 0012 parameters can be found in [19].

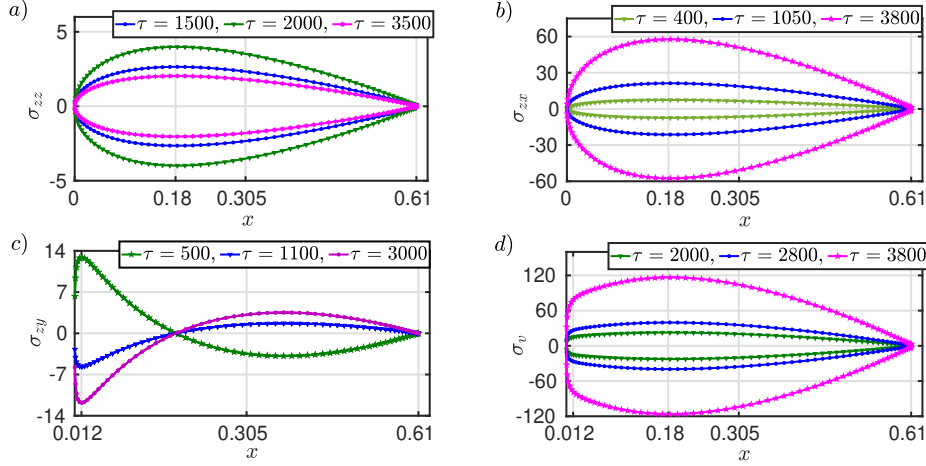


Figure 14: Variation of (a) σ_{zz} , (b) σ_{zx} , (c) σ_{zy} , and (d) σ_v , along the chord length x (meters). All the stresses are in MPa.

627 Since both torsional and bending stresses act simultaneously, the loading is multiaxial. An
 628 approximate method to convert the multiaxial stresses to a uniaxial state of stress, ‘signed von
 629 Mises criterion’ is implemented here, which is given as,

$$\sigma_v = \sqrt{\frac{(\sigma_{xx} - \sigma_{yy})^2 + (\sigma_{yy} - \sigma_{zz})^2 + (\sigma_{zz} - \sigma_{xx})^2 + 6(\sigma_{xy}^2 + \sigma_{yz}^2 + \sigma_{zx}^2)}{2}}. \quad (19)$$

630 Here, the sign of the von Mises stress is taken as that of maximum principal stress. Since the system
 631 responses are random in nature, obtained time histories of bending stress ($\sigma_{zz}(\tau)$), torsional stresses
 632 ($\sigma_{zx}(\tau)$ and $\sigma_{zy}(\tau)$) and von Mises stress ($\sigma_v(\tau)$) are also random. RFC algorithm given by Rychlik
 633 [32] is implemented to extract the load levels and turning points from random stress time histories.
 634 A MATLAB based ‘WAFO toolbox’ is utilized to calculate the RFC and corresponding damage
 635 values [56] using the Miner’s rule [33].

636 4.1. Estimation of stresses

637 For fatigue damage analysis, estimation of critical points or the locations of maximum stresses
 638 in both bending and torsional modes are required. To that end, bending and torsional stresses are
 639 calculated individually at arbitrarily chosen nondimensional time instants along the chord length.
 640 It is observed in Fig. 14(a) that σ_{zz} is maximum at $x = 0.18$ m, measured from the leading edge,
 641 which corresponds to the location of maximum airfoil thickness ($y = 0.037$ m). σ_{zy} is found to be
 642 maximum at $x = 0.012$ m which is a point close to the leading edge (see Fig. 14(b)) and the airfoil
 643 thickness at this location is $y = 0.015$ m. σ_{zx} is found to be maximum at $x = 0.18$ m, which again
 644 corresponds to the location of maximum thickness of airfoil (see Fig. 14(c)). So, the two critical
 645 points on airfoil surface are obtained as $(x = 0.012$ m, $y = 0.015$ m) and $(x = 0.18$ m, $y = 0.037$
 646 m). Note that the location of critical points do not vary with time.

647 Next, the concept of signed von Mises stress is invoked to convert the multi-axial state of stress
 648 to a uniaxial state. The variation of σ_v along the chord is shown in Fig. 14(d). It is observed that
 649 σ_v increase rapidly until a chord length of 0.012 m (the location of maximum σ_{zy} developed) and
 650 continues to increase albeit at a slower rate as chord value approaches 0.18 m, which corresponds
 651 to the location of maximum thickness. Beyond this location, von Mises stress gradually decreases.
 652 Thus, the point located at $x = 0.18$ m, $y = 0.037$ m is susceptible to maximum von Mises stress and
 653 treated as the only critical point in this study.

654 4.1.1. Developed stresses under deterministic flow

655 Stress time histories are generated under deterministic inflow conditions by calculating the
 656 stresses at the critical point. Under deterministic flow, the stress cycles are time-invariant and

Table 2: Stress amplitude (in MPa) of σ_{zz} , σ_{zx} , σ_{zy} and σ_v under deterministic flow conditions.

Aeroelastic model	U	σ_{zz}	σ_{zx}	σ_{zy}	σ_v
Attached flow/ nonlinear structure	6.6	3.64	18.11	0.17	29.75
	7.0	4.81	22.85	0.17	39.53
Nonlinear aerodynamics/ linear structure	6.6	3.12	28.39	0.20	49.61
	7.0	2.70	32.20	0.23	55.83
Nonlinear aerodynamics/ nonlinear structure	6.6	2.64	26.55	0.19	45.8
	7.0	2.10	28.51	0.20	49.28

657 have a constant stress amplitude. Amplitudes of bending, torsion, and von Mises stress cycles are
658 shown in Table 2, for $U_m = 6.6$ and 7, respectively. For nonlinear structures under attached flow
659 conditions, stress amplitudes increase with the flow speed. For the other two cases of nonlinearity,
660 all the stress amplitudes are proportional to flow speed except the bending stresses, which is due to
661 high amplitude plunge responses during the aperiodic regime. It is observed that the amplitude of
662 σ_{zy} is almost negligible as compared to that of σ_{zx} . Also, amplitude of σ_{zz} is significantly small as
663 compared to σ_{zx} . Thus, the resultant von Mises stresses are mainly contributed by σ_{zx} . Bending
664 stresses are plunge dominant and found to be highest when the flow is attached and the structure
665 possessing cubic hardening nonlinearity in pitch, which is due to linearity in plunge stiffness. On
666 the other hand, torsional stresses are highest under nonlinear aerodynamics and with linear structure,
667 owing to the pitch dominant oscillations under dynamic stall event [1]. Since σ_{zx} has greater
668 contribution in determining σ_v , as compared to σ_{zz} , the amplitude of σ_v is highest under nonlinear
669 aerodynamics for a linear structure. Incorporating cubic hardening nonlinearity in pitch results in
670 reduced torsional stresses and hence the resulting von Mises stresses also reduce significantly. In
671 field conditions, stress cycles are random. Hence, a more detailed analysis is presented next, in
672 which stresses developed under the fluctuating inflow of different time scales and intensities are ana-
673 lyzed. However, the results obtained under deterministic inflow are important as the isolated effect
674 of different nonlinearities on bending and torsional stresses is explicitly observed.

675 4.1.2. Developed stresses under stochastic flow

676 Akin to aeroelastic response analysis, stresses time histories under stochastic flow conditions
677 are obtained for three time scales ‘Type A’, ‘Type B’ and ‘Type C’ at intensity $\sigma = 0.1, 0.2$ and
678 0.3, at constant intervals of mean flow speeds (U_m) from 5 to 7. It is observed that the maximum
679 amplitudes of resultant random stress cycles are obtained at $U_m = 7$ and $\sigma = 0.3$, which are presented
680 in Table 3 and Fig. 15. Table 3 shows the maximum stress values from the random time histories
681 of σ_{zz} , σ_{zx} , σ_{zy} and σ_v along with the number of RFC. Similar to deterministic inflow conditions,
682 torsional stresses are predominant under stochastic inflow conditions as well. It is noted that stresses
683 developed under stochastic inflow are significantly higher than those under deterministic inflow. It
684 should be noted that the maximum stress values in all the cases are much below the yield strength
685 of the material (250 MPa). Developed stresses are observed to be highest when the structure is
686 linear and nonlinearity is solely aerodynamic, and lowest when the nonlinearity is solely structural.
687 The combined presence of structural nonlinearity into aerodynamic nonlinearity reduces the stress
688 amplitude and requires lesser magnitude stress cycles. It is evident that the longer the time scale,
689 the higher the amplitude of stress cycles. Under ‘Type C’ inflow, the stress amplitudes are much
690 higher than those under the other two inflow types. However, there are distinct regimes of zero stress
691 levels as well. On the contrary, ‘Type A’ inflow, having the shortest time scale among three cases,
692 gives rise to relatively lower amplitude random stress cycles, but there is no well-defined regime
693 of zero stress levels. Upon estimating the RFC of these stress cycles, it is seen that the shorter
694 the time scale, the higher are the rainflow cycles counts, which means higher the number of load
695 levels. Prediction of relative fatigue damage at different time scales from stress time histories alone

696 is challenging. Therefore, a damage rule has been adopted in section 4.2.

697 4.2. Fatigue damage estimation

698 In this section, fatigue damage is obtained using LDAR from resulting von Mises stresses. The
 699 RFC algorithm described in subsection 2.6 is used to estimate the number of rainflow cycles from
 700 each von Mises stress time history. If t_k be the time of the k^{th} local maxima, corresponding rainflow
 701 amplitude for any k^{th} cycle is given as $s_k^{RFC} = H_k - L_k^{RFC}$ (see Fig. 5). The damage at time t is
 702 given as [56]

$$fd = K \sum_{t_k \leq t} (s_k^{RFC})^\beta. \quad (20)$$

703 where K and β are material constants, which are estimated from Fig. 13. Damage values are
 704 calculated by systematically varying the flow speed under deterministic and stochastic conditions.
 705 Since the stochastic inflow is modelled as Gaussian random process, assumption of ergodicity can
 706 be considered while calculating the random stresses. It is worth mentioning that all the damage
 707 values will numerically vary for different structural and flow parameters as well as for different
 708 damage criteria. However, comparative inferences can be drawn from fatigue data to understand
 709 the effect of various factors like the type of nonlinearity, flow speed, time scale, and intensity of flow
 710 fluctuations on structural damage.

711 4.2.1. Fatigue damage under deterministic conditions

712 Under deterministic conditions, the damage is estimated for nondimensional flow speed $U = 5-7$
 713 for three nonlinear models undertaken in the present study and are presented in Fig. 16. Under
 714 deterministic flow, the model having a nonlinear structure under attached flow conditions has zero
 715 fatigue damage below $U = 6.3$, as the structure has a fixed point response in that regime. Similarly,
 716 under dynamic stall conditions, linear and nonlinear models have zero damage values below U
 717 $= 5.7$. The order of damage is seen to be increasing with flow speed. It is found highest for the
 718 model having aerodynamic nonlinearity and linear structure and least for the model with a nonlinear
 719 structure under attached flow conditions. It is observed that the damage caused by pure aerodynamic
 720 nonlinearity is approximately 30 times more than that caused by pure structural nonlinearity, while
 721 coupling the structural nonlinearity into the aerodynamic nonlinearity almost halves the fatigue
 722 damage for the structural parameters considered in this study. Thus cubic hardening structural
 723 nonlinearity plays a significant role in reducing fatigue damage. **This is attributed to the fact**
 724 **that the structure becomes stiffer with deformation due to the inherent property of**
 725 **structure possessing a hardening type of nonlinearity.** On the other hand, nonlinearities
 726 arising from the flow are seen to aggravate the fatigue damage severely. A detailed fatigue-based
 727 design is thus essential for aeroelastic systems, such as blades of wind turbines and helicopters, which
 728 are highly prone to dynamic stall phenomenon.

729 4.2.2. Fatigue damage under stochastic conditions

730 Finally, fatigue damage analysis is done for different nonlinear systems under the effect of fluctu-
 731 ating inflow. Due to the stochastic modeling, actual fatigue damage incurred due to aeroelastic
 732 instability is always uncertain. However, statistical data can be collected by changing several stochas-
 733 tic parameters like time scale and fluctuation intensity. Under stochastic inflow, fatigue damage is
 734 found to be higher as compared to that under deterministic flow.

735 For nonlinear structure under attached flow, variation in fatigue damage values under ‘Type A’
 736 (Fig. 17(a)) and ‘Type B’ (Fig. 17(b)) inflow, are seen to be less affected by intensity variation as
 737 compared to those under ‘Type C’ inflow (Fig. 17(c)). For $\sigma = 0.1$, the damage values are only
 738 slightly higher than fatigue under deterministic flow while for $\sigma = 0.3$, the damage is 100 times
 739 higher. Also at $\sigma = 0.3$, significant damage is accumulated even below flutter speed which is a point
 740 of concern from the structural health perspective. Under ‘Type C’ inflow, maximum fatigue damage
 741 obtained at $\sigma = 0.3$ is almost 30 times of that obtained at $\sigma = 0.1$, while for ‘Type A’ inflow, its
 742 only twice as high at $\sigma = 0.3$ as compared to that at $\sigma = 0.1$.

743 For the model with pure aerodynamic nonlinearity, the damage variation is shown for ‘Type A’,
 744 ‘Type B’ and ‘Type C’ inflow in Fig. 18. Accumulated damage is seen to be almost 60 times higher

Table 3: Maximum value (in MPa) of σ_{zz} , σ_{zx} , σ_{zy} , σ_v and RFC under fluctuating inflow at $\sigma = 0.3$ and $U_m = 7$.

Aeroelastic model	Inflow type	σ_{zz}	σ_{zx}	σ_{zy}	σ_v	RFC
Attached flow/nonlinear structure	'Type A'	9.48	30.39	0.21	53.00	294
	'Type B'	12.18	38.69	0.28	70.08	291
	'Type C'	12.47	52.19	0.37	91.07	284
Nonlinear aerodynamics/linear structure	'Type A'	10.18	42.16	0.28	72.17	373
	'Type B'	28.86	49.29	0.38	98.30	349
	'Type C'	28.50	88.47	0.64	158.71	303
Coupled structural/aerodynamic nonlinearity	'Type A'	13.88	39.02	0.27	66.30	406
	'Type B'	13.25	42.85	0.31	76.46	387
	'Type C'	21.49	61.19	0.44	107.06	373

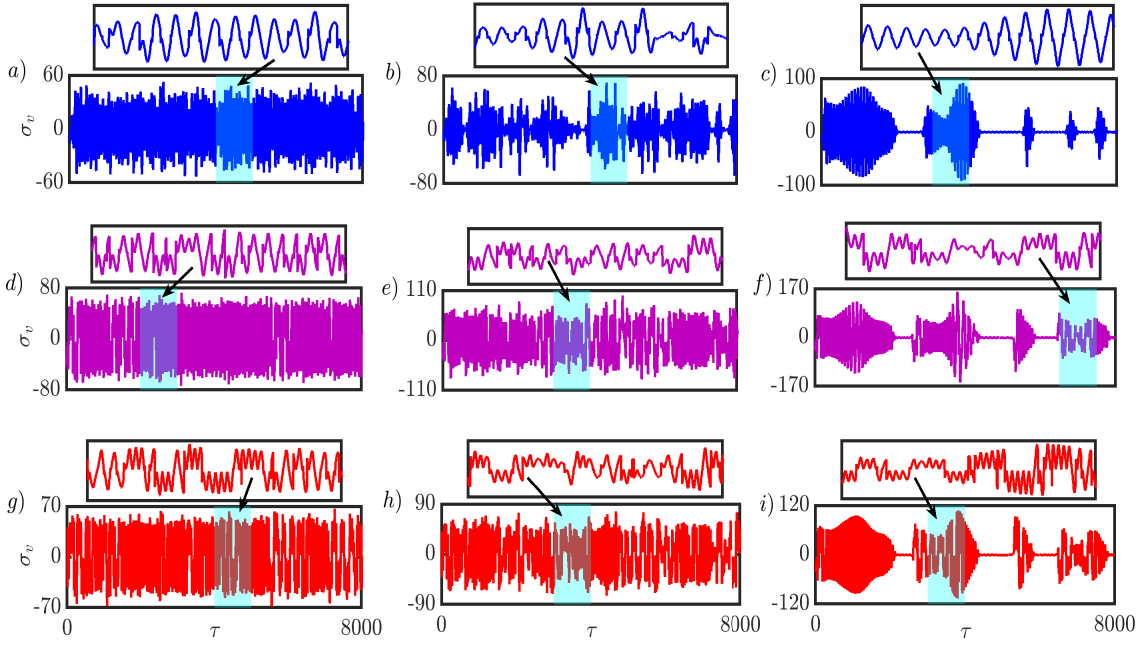


Figure 15: Sample time histories of σ_v (MPa) at $\sigma = 0.3$ and $U_m = 7$; for nonlinear structure and linear aerodynamics under (a) 'Type A' flow, (b) 'Type B' flow, and (c) 'Type C' flow; for linear structure and nonlinear aerodynamics under (d) 'Type A' flow, (e) 'Type B' flow, and (f) 'Type C' flow; and for both nonlinear structure and aerodynamics under (g) 'Type A' flow, (h) 'Type B' flow, and (i) 'Type C' flow.

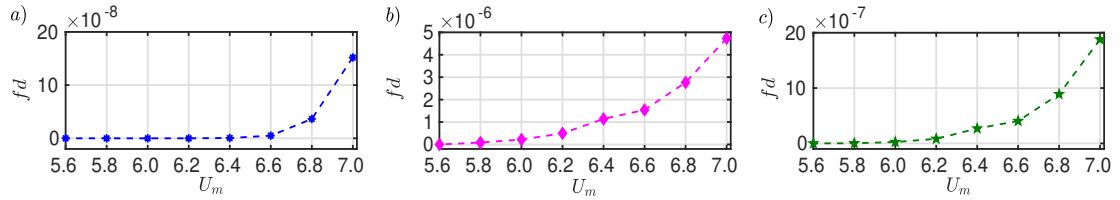


Figure 16: Accumulated damage values under non-fluctuating inflow for (a) Nonlinear structure under attached flow conditions, (b) Linear structure under nonlinear aerodynamic conditions, and (c) Nonlinear structure under nonlinear aerodynamic conditions.

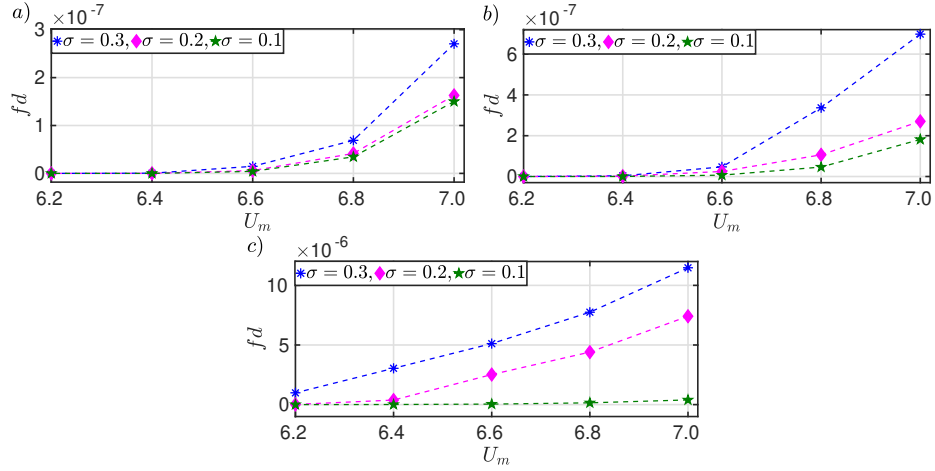


Figure 17: Accumulated damage values under attached flow conditions with the structure possessing cubic hardening nonlinearity in pitch for, (a) 'Type A' inflow, (b) 'Type B' inflow, and (c) 'Type C' inflow.

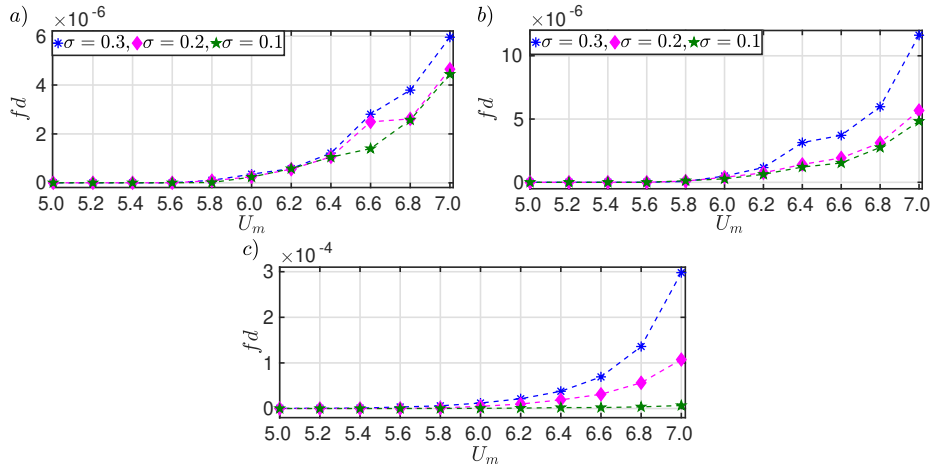


Figure 18: Accumulated damage values under dynamic stall conditions for a linear structure for, (a) 'Type A' inflow, (b) 'Type B' inflow, and (c) 'Type C' inflow.

745 for 'Type A' inflow at $U_m = 7$ and $\sigma = 0.3$, as compared to damage values under deterministic flow
 746 conditions. While as compared to damage obtained from the model possessing structural nonlinearity
 747 under attached flow conditions, the corresponding damage is almost 30 times higher. This indicates
 748 the severity of stall flutter problem in the aeroelastic systems, which can be much more dangerous
 749 in the presence of material defects like cracks and aging effects. It is quite unrealistic to have
 750 an aeroelastic system without any structural nonlinearity. However, the present model with linear
 751 structure demonstrates the isolated effect of aerodynamic nonlinearity on its structural health. Next,
 752 a more realistic set of fatigue damage results is provided when a coupling between aerodynamic and
 753 structural nonlinearity is considered.

754 Structural stiffness is a major design aspect for aeroelastic systems from both static and dynamic
 755 analysis perspectives. For a linear structure, flutter amplitude is diverging, and a hardening nonlin-
 756 earity in stiffness limits the diverging oscillations to LCOs [3]. In the present study, a similar effect
 757 of cubic hardening pitch nonlinearity is observed. When cubic hardening nonlinearity is coupled
 758 with aerodynamic nonlinearity, the amplitude of stall flutter LCOs is significantly reduced. Since
 759 the present study considers only pitch and plunge deformations to calculate the stresses, the stresses
 760 are also reduced significantly by coupling structural nonlinearity to the aerodynamic nonlinearity.
 761 However, the number of load levels is also higher in a coupled nonlinear system than in isolated
 762 aerodynamic nonlinearity. Hence, a fatigue damage analysis is needed to understand the actual im-

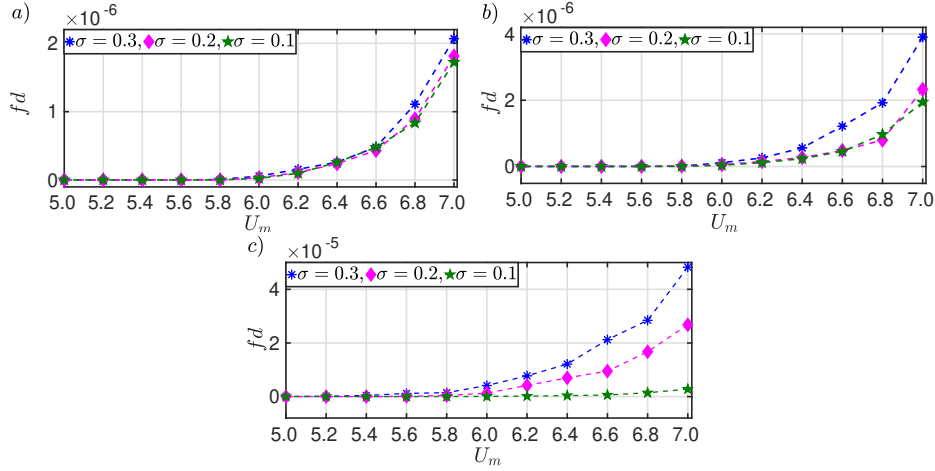


Figure 19: Accumulated damage values under dynamic stall conditions for a nonlinear structure for, (a) ‘Type A’ inflow, (b) ‘Type B’ inflow, and (c) ‘Type C’ inflow.

763 pact of structural nonlinearity on a system governed by nonlinear aerodynamic loads. Under ‘Type
 764 A’ inflow (Fig. 19(a)), the damage values are almost similar to those obtained under deterministic
 765 conditions and are almost one-third of those obtained for the system under pure aerodynamic non-
 766 linearity. Under ‘Type B’ inflow (Fig. 19(b)), the damage values are slightly higher, particularly
 767 at $\sigma = 0.3$, the damage values almost double as compared to those under ‘Type A’ inflow for same
 768 intensity. Damage values are very high under ‘Type C’ inflow (Fig. 19(c)) as compared to those
 769 under the other two types of inflow, and at $\sigma = 0.3$, the values reach almost 20 times higher as
 770 compared to those obtained under deterministic flow for the same nonlinear model. However, the
 771 damage values under ‘Type C’ inflow for a system with coupled structural and aerodynamic non-
 772 linearity are significantly reduced than that with pure aerodynamic nonlinearity. At $\sigma = 0.3$, the
 773 damage incurred by the system under nonlinear aerodynamic load is reduced almost to $1/6^{th}$ with
 774 the addition of cubic hardening nonlinearity in structure.

775 So far, from the numerical simulations, we observe the route to stall flutter in aeroelastic sys-
 776 tems depending on the source of nonlinearity and nature of the on-coming wind flows (deterministic/
 777 stochastic). For comparison purposes, classical flutter scenarios are as well invoked. From the
 778 discerned routes to stall flutter, we compute the fatigue damage incurred under a variety of scenar-
 779 ios. At the interim juncture, we note that the fatigue damage is consistently high for aerodynamic
 780 nonlinearities (*i.e.* dynamic stall conditions) irrespective of the deterministic/stochastic nature of
 781 the input flow. It is to be reminded to the reader that in hitherto studies, minimal attention has
 782 been devoted towards both resolving the intermittency route to stall flutter as well as the structural
 783 safety aspect of the same. To glean further into stall-induced fatigue damages in aeroelastic systems,
 784 a comparison of our numerical findings with wind tunnel experiments becomes highly necessary.

785 5. Experimental investigations into stall induced fatigue damage

786 A preliminary investigation into stall flutter-induced fatigue damage estimated through wind
 787 tunnel experiments is presented in this section. The experiments are performed on a NACA 0012
 788 airfoil in a low speed Eiffel type wind tunnel with closed test section (see Fig. 20 (a)). A photograph
 789 of the experimental setup inside the wind tunnel test section (dimensions 0.8 m x 0.8 m x 1.2 m)
 790 is shown in Fig. 20(b). The airfoil has a span of 0.5 m, chord length of 0.1 m, and is mounted
 791 horizontally at the quarter chord in the experimental mechanism. The mechanism is akin to that in
 792 Venkatramani *et al.* [53, 27] and its details are not repeated here for brevity sake. A static experiment
 793 is performed to obtain load vs deflection curves for plunge (Fig. 20(c)) and pitch (Fig. 20(d)) stiffness,
 794 respectively and both the modes show approximately linear stiffness behaviour. A pair of laser
 795 displacement sensors having a Wenglor make, and a resolution of one micron, and a displacement
 796 range of 50-350 mm is used to obtain the pitch and plunge displacements of the airfoil. A pair of

Table 4: The structural parameters for the experiment. m_y and m_α represent the total moving mass in plunge and pitch respectively and f_y and f_α represents the natural frequency of plunge and pitch mode, respectively (estimated from static experiments).

Parameter	m_y (kg)	m_α (kg)	f_y (Hz)	f_α (Hz)	a_h	I_α (kg-m ²)
Value	1.908	0.937	2.28	4.01	-0.5	0.0017

797 Delta HD 4V3 TS3 type air velocity sensors are used to the perpetual acquisition of the flow velocity
798 in the wind tunnel test section. Additionally, a stand-alone hot wire anemometer is used to monitor
799 the flow velocities inside the test section. An ATALON data acquisition system is used for acquiring
800 the flow-velocity and the displacement values from the laser sensors as well. The maximum speed
801 achievable in the wind tunnel is approximately 25 m/s. By installing remote controllers over the
802 tunnel fan, the direction of wind flow can be changed from suction to blowing mode.

803 Under the suction mode of operation, the flows are largely sterile and free from fluctuations
804 (holding true both for empty test section and in the presence of experimental setup - albeit that
805 the latter case understandably gives rise to a larger turbulence intensity). The turbulence intensity
806 under suction mode - obtained from flow data measured using hot-wire anemometers - is less than
807 1% in the empty section. The blowing mode of tunnel fan operation, on the other hand, gives rise
808 to flows that do not pass via honeycomb meshes, and rather give rise to fluctuating input flows to
809 the test section. Further details about the same can be found in Venkatramani *et al.* [53, 27]. While
810 anemometers help us obtain turbulence intensities at different points, we refrain from explicitly
811 quoting the turbulence intensity in this case as we feel that the full information of flow fluctuations
812 in the test section can be best discerned from particle image velocimetry (PIV) - which is unavailable
813 with us. In wake of turbulence levels, varying point to point in the test section, as well as varying for
814 increasing levels of mean flow speed, we feel it is premature and incomplete to provide turbulence
815 levels in this case. However, given that the focus of the study involves both deterministic (sterile)
816 and stochastic (fluctuating) flows, we show two sample wind time histories below for the sake of
817 readers' clarity. As shown in Fig. 21, the flow data obtained under suction conditions at speed (V)
818 = 14.11 m/s is predominantly invariant with time. On the other hand, the flow time history at
819 mean speed (V_m) = 14.16 m/s measured under blowing conditions shows much higher fluctuations.
820 The turbulence intensity for this case, computed in a simplistic manner as the ratio of the variance
821 of the random process upon the mean value, gives an intensity of 2.65%. Note that the wind profile
822 qualitatively and quantitatively changes at various points inside the test section and also varies
823 considerably with an increase in the mean flow speed. However, quantifying the same is beyond the
824 scope of the present study.

825 Subsequent to characterizing the static parameters associated with the experimental framework
826 (see Table 4), we carry out dynamic experiments under suction mode of fan operation. The flow
827 speed (V) is varied systematically from zero to the critical flow speed in which we encounter the
828 onset of LCOs. The initial angle of attack of the airfoil is 6°, which is well below the static stall
829 angle of NACA 0012 [16]. Large amplitude LCOs is observed at $V = 13.82$ m/s; see Figs. 22(a) and
830 22(b). The LCO amplitudes for the pitch DoF are very high and possibly can be attributed to flow
831 separation and dynamic stall [7, 12, 8]. The frequencies of pitch and plunge oscillations coalesce at
832 the pitch natural frequency (= 4.01 Hz); see Fig. 22(c). This confirms that the oscillations are pitch
833 dominant and can be characterized as stall flutter. It's worth mentioning that the pitch and plunge
834 springs behave linearly (see Fig. 20(c) and Fig. 20(d)) and hence the contribution of structural
835 nonlinearity can be assumed as insignificant.

836 Figure 23 shows the pitch responses of airfoil under blowing conditions from the velocity range
837 13.18 - 15.97 m/s. It is observed that airfoil undergoes random oscillations of significant amplitudes
838 at $V = 13.18$ m/s (Fig. 23(a)), which is well below the flutter speed (13.82 m/s). Upon increasing
839 the speed to 14.16 m/s (Fig. 23(b)), the random LCOs grow in amplitude, and at 14.93 m/s, large
840 amplitude random LCOs are observed (Fig. 23(c)). Finally at 15.97 m/s, the amplitude of the

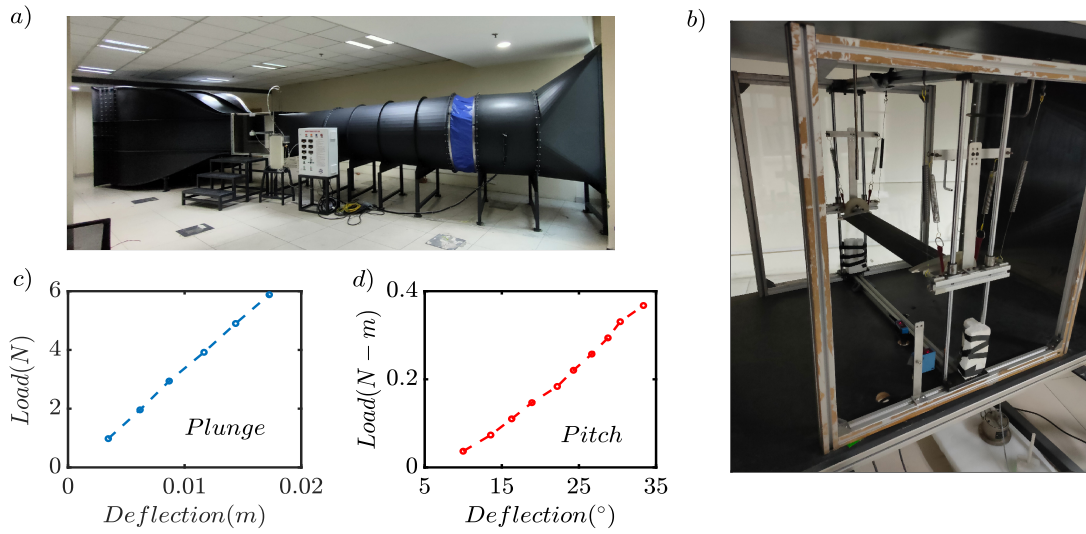


Figure 20: Photographs of the experimental setup; a) Wind tunnel; b) NACA 0012 airfoil in wind tunnel test section along with sensors. Fig. (c) and Fig. (d) represent the load vs deflection plot for plunge and pitch stiffness respectively, which are estimated from the static experiments.

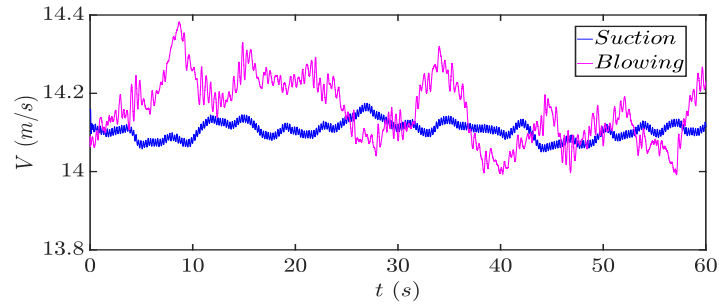


Figure 21: Sample time history of flow variation under suction and blowing conditions.

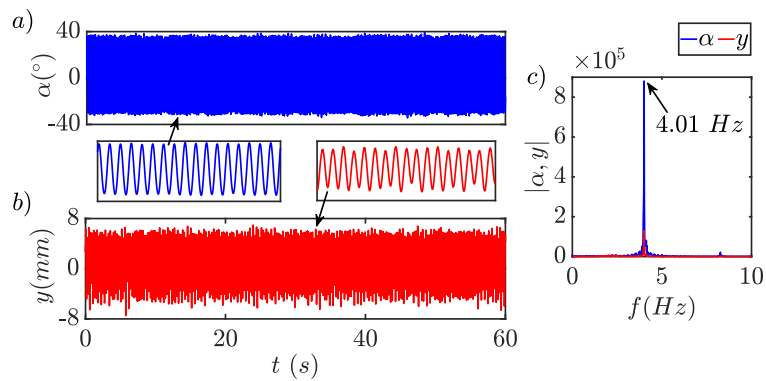


Figure 22: Experimentally obtained responses of NACA 0012 airfoil under suction conditions at stall flutter onset ($V = 13.82$ m/s); a) Pitch response, b) Plunge response, c) Coalescence of pitch and plunge frequencies at pitch natural frequency confirming pitch dominant LCOs.

Table 5: Maximum value of σ_v (in MPa) and accumulated fatigue damage values calculated from experimentally obtained airfoil responses using experimental structural parameters (0.5 m span and 0.1 m chord).

Operating conditions	flow speed	σ_v	fd
Suction	13.82	215.94	0.50
Suction	14.63	221.35	0.55
Blowing	13.18	50.11	2.32×10^{-8}
Blowing	14.16	62.43	1.70×10^{-7}
Blowing	14.93	170.94	1.40×10^{-2}
Blowing	15.97	211.24	0.19

random LCOs further increases and becomes more uniform (Fig. 23(d)). Akin to section 4, the stress time histories are obtained from airfoil responses using the same methodology i.e. the airfoil is assumed to be a cantilever structure of 0.1 m chord and 0.5 m span subjected to multiaxial loading. The material properties are same as mentioned in Section 4. Obtained von Mises stresses are presented in Fig. 24. The maximum values of von Mises stresses at various flow speeds are tabulated in Table 5, which are below the material yield strength and their order is similar to those obtained numerically, albeit slightly higher. For the numerical model with pure aerodynamic nonlinearity, the maximum von Mises stress is 158.71 MPa (see Table 3), while for experimentally observed stall induced instability, the maximum von Mises stress is obtained as 221.35 MPa (see Table 5). One of the reasons for higher stresses obtained in experimental framework is perhaps the size of the structure. Since performing wind tunnel experiments in such a big structure, akin to the numerical model, is beyond the capacity under current experimental facilities, we take a miniature blade model and perform similar analysis.

Next, we embark into the estimated fatigue damage obtained from the von Mises stresses. Here we present two cases under suction conditions, and four cases under blowing conditions. The damage is calculated from 60 sec stress data and is presented in Table 5. Although there is significant damage under blowing conditions at $V_m = 13.18$ m/s, which is below the flutter point (13.82 m/s), we see that the fatigue damage caused under suction condition is much higher. Hence for current set of experimental conditions, deterministic inflow (suction) causes more damage as compared to stochastic inflow (blowing). Its worth mentioning that the fatigue damage is highly dependent upon the probabilistic markers namely intensity and time scale of stochastic inflow as shown in subsection 4.2.2. In fact, observing Fig. 16(b) and Fig. 18(a) from numerical analysis, which are cases of pure aerodynamic nonlinearity (akin to experimental case), we see that the fatigue damage values under deterministic conditions (Fig. 16(b)) are higher than those under stochastic conditions (Fig. 18) specifically for low intensity and short time scale conditions, which is possibly the case under blowing experiments also and hence we observe lower fatigue than the suction conditions.

6. Concluding remarks

This study is focused on estimating the effect of nonlinearity originating from various sources under stochastic flow conditions on the aeroelastic responses and associated fatigue damage. Nonlinearity arising from the structure is modeled as cubic hardening pitch stiffness; whereas, the aerodynamic nonlinearity is modeled using LB dynamic stall model. Uncertainties in the oncoming flow are incorporated by modeling the inlet velocity as a stochastic process using KLE with different time scales and intensities. From the same, the following salient findings emerge.

- First, the dynamical signatures of the system under deterministic and stochastic flow conditions are presented by considering isolated cases of nonlinearities and then by studying the combined effects. Under deterministic flow, the bifurcation plots show distinct dynamical behavior under different types of nonlinearity. For a nonlinear structure under attached flow conditions, fixed point response transitions to LCO via a Hopf bifurcation, while for a linear structure under

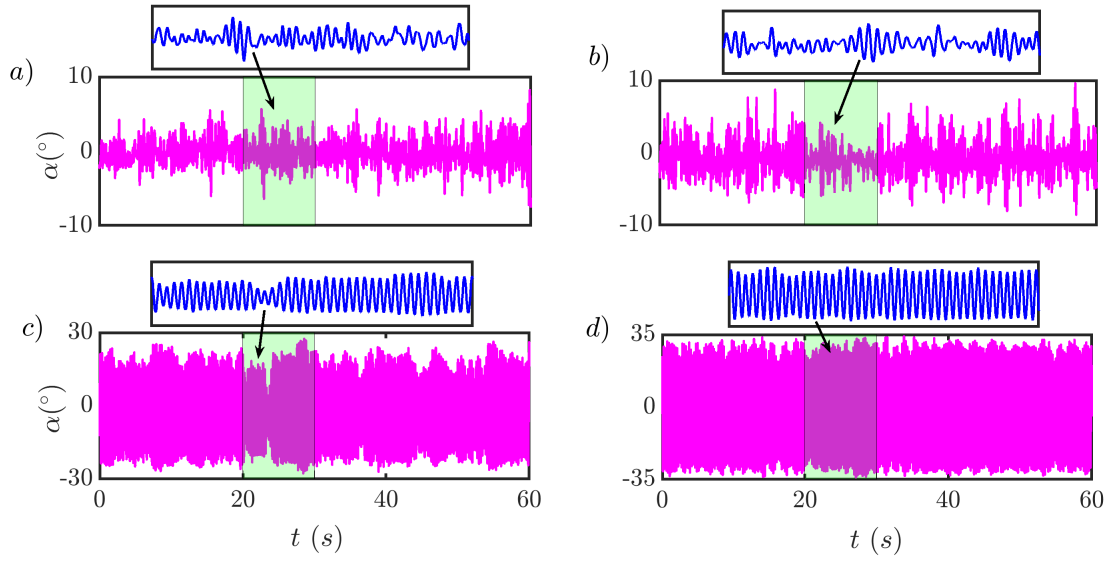


Figure 23: Experimentally obtained pitch responses (in radians) of NACA 0012 airfoil under blowing conditions at; a) $V = 13.18$ m/s, b) $V = 14.16$ m/s, c) $V = 14.93$ m/s, d) $V = 15.97$ m/s, showing transitions from random LCOs to fully developed LCOs as the flow speed is increased

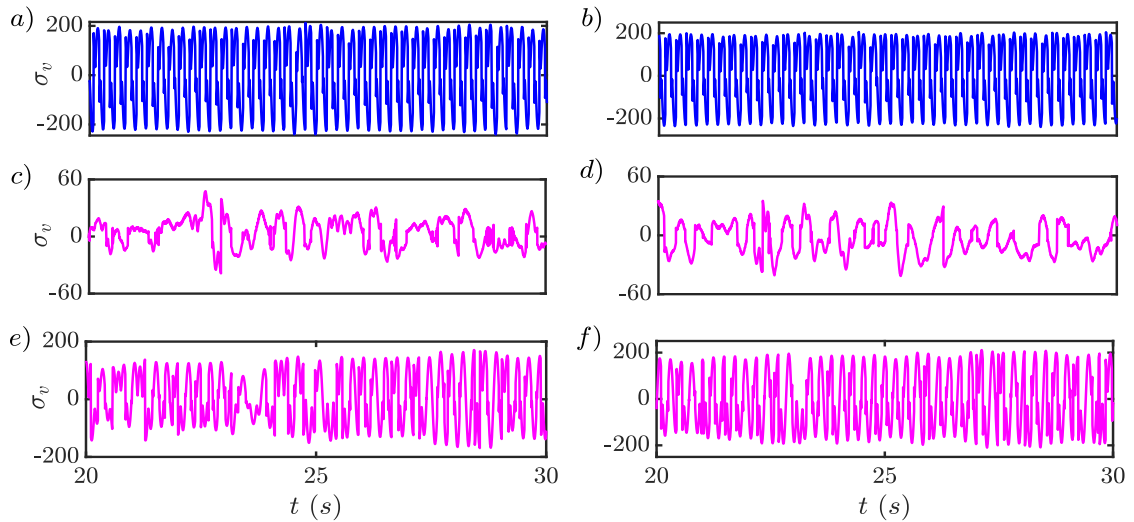


Figure 24: Sample time histories of von Mises stresses calculated from experimentally obtained pitch-plunge responses; under suction conditions a) at $V = 13.82$ m/s and b) at $V = 14.63$ m/s; under blowing conditions c) at $V = 13.18$ m/s, d) at $V = 14.16$ m/s, e) at $V = 14.93$ m/s and f) at $V = 15.97$ m/s.

879 aerodynamic nonlinearity, stall induced aperiodic oscillations presage LCOs. Under combined
880 effects of structural and aerodynamic nonlinearity, distinct regimes of period-1, period-3, and
881 aperiodic oscillations are observed prior to the onset of stall-induced LCOs.

882 • Accounting for random fluctuation in the flow gives rise to far more complex signatures, and
883 the qualitative nature of the responses gets largely altered compared to the deterministic
884 cases. The responses under fluctuating flow conditions are governed by the time scale and
885 intensity of fluctuating inflow. Under short time scale input flows, the response signatures
886 depict “burst-type” intermittency. Under long time scale input flows, the responses exhibit
887 an “on-off” intermittency phenomenon. Thus, distinct signatures are present in aeroelastic
888 responses under different nonlinearity and stochastic inflow conditions.

889 • Using this as an impetus, the system is next investigated from the standpoint of structural
890 safety by estimating the fatigue damage accumulation in the presence of different nonlinearities
891 and inflow conditions. Under stochastic conditions, it is observed that a cubic hardening
892 nonlinear stiffness behavior in the structure can potentially reduce the magnitude of induced
893 stresses. At the same time, the presence of aerodynamic nonlinearity has an adverse effect on
894 stress levels.

895 • Next, it is demonstrated that the fatigue damage depends on the mean flow speed, fluctuation
896 intensity, and correlation length of stochastic inflow. A comparison between damage-velocity
897 plots for different nonlinear models shows much higher damage values when nonlinearity is
898 purely aerodynamic than cases with purely structural or coupled nonlinearity.

899 • Finally, we analyze stall-induced instability and subsequent fatigue damage in the deterministic
900 and stochastic frameworks through wind tunnel experiments. Under suction conditions, large-
901 amplitude LCOs are obtained, which are characterized as stall flutter from frequency analysis.
902 On the other hand under blowing conditions, random LCOs are observed below the flutter
903 point which culminates into well-developed LCOs as the flow speed is increased. Specifically,
904 an intermittency route to stall flutter is observed from the experiments as well.

905 • Fatigue damage analysis from experimental responses shows higher damages owing to stall-
906 induced oscillations - underscoring the larger damages incurred under torsionally dominant
907 oscillations. While the numerics specifically underscored the role of noise intensity and time
908 scale of the flow fluctuations over the fatigue accumulation, the framework of experiments was
909 restrictive for us to depict the same.

910 Indeed, the change of noise intensity and scales of input stochastic wind, and in-turn measuring
911 it demand stand alone attention. Nevertheless, both the numerical and experimental findings
912 concur that stall-induced oscillations can impart substantial fatigue damage to the aeroelastic
913 structure.

914 Given that nonlinearities and random temporal flows are ubiquitous in a suite of aeroelastic
915 problems such as aircraft wings, wind turbine blades, helicopter blades, and even in problems in-
916 volving bridge-decks, the findings documented in this study carry relevance from the purview of
917 structural safety. Although, the aeroelastic community has heuristically been aware of the impact of
918 stochasticity and nonlinearities in jeopardizing structural safety, minimal efforts to quantify the same
919 are available so far. In that retrospect, this is perhaps the first study to systematically investigate
920 the effect of different nonlinearities and stochastic conditions on fatigue damage of the aeroelastic
921 system *visa a vis* the response dynamics. However, it must be cautioned to the reader that the
922 practicability of the findings presented here to in-field problems involving diverse flow-structural in-
923 teractions might require further investigations. **Present study considers only cubic hardening
924 nonlinearity in structure. Similar studies considering structural nonlinearities giving
925 raise to subcriticality is indeed an interesting topic and requires a separate study. The
926 complexities arising in fatigue damage estimation due to coexisting attractors due to
927 subcriticality is interesting problem to address. The authors aim for the same in a
928 subsequent study.** This study, as a starting step, is undertaken for a prismatic blade model under

929 uniformly distributed fluid loading with isotropic material properties. Extending the present find-
930 ings to anisotropic wings (akin to [57]) and even to isotropic structures with material uncertainties
931 (akin to [19]) requires fresh investigations. **The robustness of the analysis can be improved**
932 **by using CFD solvers to incorporate effects of 3D flow-field behaviour as well as finite**
933 **element based solvers to capture aeroelastic responses more accurately.** Furthermore,
934 the present study restricts the flow fluctuations to the axial direction. However, it is typical in the
935 aeroelastic community to assign a larger for the random vertical gust [47] over both the response
936 dynamics and the associated impact on structural health. These are very interesting open problems
937 to be taken up by the authors in the future.

938 Acknowledgments

939 The authors gratefully acknowledge the funding received from Science and Engineering Research
940 Board (SERB) - start up research grant (SRG-2019- 000077) towards this research.

941 Declaration of competing interest

942 The authors declare that they have no known competing financial interests or personal relation-
943 ships that could have appeared to influence the work reported in this paper.

944 References

- 945 [1] G. Dimitriadis, Introduction to nonlinear aeroelasticity, John Wiley & Sons, 2017.
- 946 [2] C. Riso, C. E. Cesnik, B. I. Epureanu, Output-based flutter bifurcation forecasting in nonlinear
947 fluid-structural systems with multiple varying parameters, *Journal of Fluids and Structures* 101
948 (2021) 103201.
- 949 [3] B. Lee, S. Price, Y. Wong, Nonlinear aeroelastic analysis of airfoils: bifurcation and chaos,
950 *Progress in Aerospace Sciences* 35 (3) (1999) 205–334.
- 951 [4] S. Li, L. Caracoglia, Surrogate model monte carlo simulation for stochastic flutter analysis of
952 wind turbine blades, *Journal of Wind Engineering and Industrial Aerodynamics* 188 (2019)
953 43–60.
- 954 [5] L. Wang, R. Quant, A. Kolios, Fluid structure interaction modelling of horizontal-axis wind
955 turbine blades based on cfd and fea, *Journal of Wind Engineering and Industrial Aerodynamics*
956 158 (2016) 11–25.
- 957 [6] L. Wang, X. Liu, A. Kolios, State of the art in the aeroelasticity of wind turbine blades:
958 Aeroelastic modelling, *Renewable and Sustainable Energy Reviews* 64 (2016) 195–210.
- 959 [7] G. Dimitriadis, J. Li, Bifurcation behavior of airfoil undergoing stall flutter oscillations in low-
960 speed wind tunnel, *AIAA Journal* 47 (11) (2009) 2577–2596.
- 961 [8] D. Poirel, L. Goyaniuk, A. Benaissa, Frequency lock-in in pitch–heave stall flutter, *Journal of*
962 *Fluids and Structures* 79 (2018) 14–25.
- 963 [9] S. Sarkar, H. Bijl, Nonlinear aeroelastic behavior of an oscillating airfoil during stall-induced
964 vibration, *Journal of Fluids and Structures* 24 (6) (2008) 757–777.
- 965 [10] U. Galvanetto, J. Peiro, C. Chantharasenawong, An assessment of some effects of the nons-
966 moothness of the leishman–beddoes dynamic stall model on the nonlinear dynamics of a typical
967 aerofoil section, *Journal of Fluids and Structures* 24 (1) (2008) 151–163.
- 968 [11] R. M. G. d. Vasconcellos, D. d. A. Pereira, F. D. Marques, Characterization of nonlinear
969 behavior of an airfoil under stall-induced pitching oscillations, *Journal of Sound and Vibration*
970 372 (2016) 283–298.

- 971 [12] C. R. dos Santos, D. A. Pereira, F. D. Marques, On limit cycle oscillations of typical aeroe-
972 lastic section with different preset angles of incidence at low airspeeds, *Journal of Fluids and*
973 *Structures* 74 (2017) 19–34.
- 974 [13] S. Vishal, A. Raaj, C. Bose, J. Venkatramani, Routes to synchronization in a pitch-plunge aeroe-
975 lastic system with coupled structural and aerodynamic nonlinearities, *International Journal of*
976 *Non-Linear Mechanics* (2021) 103766.
- 977 [14] R. V. Bethi, S. V. Gali, J. Venkatramani, Response analysis of a pitch-plunge airfoil with
978 structural and aerodynamic nonlinearities subjected to randomly fluctuating flows, *Journal of*
979 *Fluids and Structures* 92 (2020) 102820.
- 980 [15] H. Devathi, S. Sarkar, Study of a stall induced dynamical system under gust using the proba-
981 bility density evolution technique, *Computers & Structures* 162 (2016) 38–47.
- 982 [16] L. dos Santos, F. Marques, Nonlinear aeroelastic analysis of airfoil section under stall flutter
983 oscillations and gust loads, *Journal of Fluids and Structures* 102 (2021) 103250.
- 984 [17] P. Chaviaropoulos, Flap/lead-lag aeroelastic stability of wind turbine blade sections, *Wind*
985 *Energy: An International Journal for Progress and Applications in Wind Power Conversion*
986 *Technology* 2 (2) (1999) 99–112.
- 987 [18] F. Rasmussen, M. H. Hansen, K. Thomsen, T. J. Larsen, F. Bertagnolio, J. Johansen, H. A.
988 Madsen, C. Bak, A. M. Hansen, Present status of aeroelasticity of wind turbines, *Wind Energy:*
989 *An International Journal for Progress and Applications in Wind Power Conversion Technology*
990 6 (3) (2003) 213–228.
- 991 [19] S. Venkatesh, S. Sarkar, I. Rychlik, Uncertainties in blade flutter damage prediction under
992 random gust, *Probabilistic Engineering Mechanics* 36 (2014) 45–55.
- 993 [20] Y. L. Xu, T. Liu, W. Zhang, Buffeting-induced fatigue damage assessment of a long suspension
994 bridge, *International Journal of Fatigue* 31 (3) (2009) 575–586.
- 995 [21] G. Georgiou, A. Manan, J. E. Cooper, Modeling composite wing aeroelastic behavior with
996 uncertain damage severity and material properties, *Mechanical Systems and Signal Processing*
997 32 (2012) 32–43.
- 998 [22] S. Sarkar, S. Gupta, I. Rychlik, Wiener chaos expansions for estimating rain-flow fatigue damage
999 in randomly vibrating structures with uncertain parameters, *Probabilistic Engineering Mechan-*
1000 *ics* 26 (2) (2011) 387–398.
- 1001 [23] J. A. Witteveen, S. Sarkar, H. Bijl, Modeling physical uncertainties in dynamic stall induced
1002 fluid-structure interaction of turbine blades using arbitrary polynomial chaos, *Computers &*
1003 *Structures* 85 (11-14) (2007) 866–878.
- 1004 [24] B. H. Lee, L. Liu, Bifurcation analysis of airfoil in subsonic flow with coupled cubic restoring
1005 forces, *Journal of Aircraft* 43 (3) (2006) 652–659.
- 1006 [25] J. Venkatramani, S. K. Kumar, S. Sarkar, S. Gupta, Physical mechanism of intermittency route
1007 to aeroelastic flutter, *Journal of Fluids and Structures* 75 (2017) 9–26.
- 1008 [26] J. Venkatramani, S. Sarkar, S. Gupta, Intermittency in pitch-plunge aeroelastic systems ex-
1009 plained through stochastic bifurcations, *Nonlinear Dynamics* 92 (3) (2018) 1225–1241.
- 1010 [27] J. Venkatramani, S. Sarkar, S. Gupta, Investigations on precursor measures for aeroelastic
1011 flutter, *Journal of Sound and Vibration* 419 (2018) 318–336.
- 1012 [28] C. Bose, S. Gupta, S. Sarkar, Transition to chaos in the flow-induced vibration of a pitching-
1013 plunging airfoil at low reynolds numbers: Ruelle-takens-newhouse scenario, *International Jour-*
1014 *nal of Non-Linear Mechanics* 109 (2019) 189–203.

- 1015 [29] M. H. Hansen, M. Gaunaa, H. A. Madsen, A beddoes-leishman type dynamic stall model in
1016 state-space and indicial formulations, Tech. rep., Risoe National Lab., Roskilde (Denmark)
1017 (2004).
- 1018 [30] J. G. Leishman, T. Beddoes, A semi-empirical model for dynamic stall, *Journal of the American*
1019 *Helicopter Society* 34 (3) (1989) 3–17.
- 1020 [31] J. Leishman, K. Nguyen, State-space representation of unsteady airfoil behavior, *AIAA Journal*
1021 28 (5) (1990) 836–844.
- 1022 [32] I. Rychlik, A new definition of the rainflow cycle counting method, *International Journal of*
1023 *Fatigue* 9 (2) (1987) 119–121.
- 1024 [33] M. A. Miner, Cumulative damage in fatigue, *Journal of Applied Mechanics* 12 (3) (1945) A159–
1025 A164.
- 1026 [34] A. Palmgren, Die lebensdauer von kugellagern, *VDI Zeitschrift* 68 (1924) 339–341.
- 1027 [35] J. Leishman, T. Beddoes, A generalised model for airfoil unsteady aerodynamic behaviour and
1028 dynamic stall using the indicial method, in: *Proceedings of the 42nd Annual forum of the*
1029 *American Helicopter Society*, Washington DC, 1986, pp. 243–265.
- 1030 [36] R. G. Ghanem, P. D. Spanos, *Stochastic finite elements: a spectral approach*, Courier Corpo-
1031 ration, 2003.
- 1032 [37] A. Rounak, S. Gupta, Stochastic p-bifurcation in a nonlinear impact oscillator with soft barrier
1033 under ornstein–uhlenbeck process, *Nonlinear Dynamics* 99 (4) (2020) 2657–2674.
- 1034 [38] K. McAlister, S. Pucci, W. McCroskey, L. Carr, An experimental study of dynamic stall on
1035 advanced airfoil sections. volume 2. pressure and force data, Tech. rep., NASA. TM 84245
1036 (1982).
- 1037 [39] R. P. L. Nijssen, Fatigue life prediction and strength degradation of wind turbine rotor blade
1038 composites, Ph.D. thesis, Faculty of Aerospace Engineering, T.U. Delft (2006).
- 1039 [40] M. Matsuishi, T. Endo, Fatigue of metals subjected to varying stress, in: *Proceedings Kyushi*
1040 *Branch JSME*, Vol. 68, 1968, pp. 37–40.
- 1041 [41] N. Dowling, Fatigue failure predictions for complicated stress-strain histories, *Journal of Mate-*
1042 *rials* 7 (1) (1972) 71–87.
- 1043 [42] S. D. Downing, D. Socie, Simple rainflow counting algorithms, *International Journal of Fatigue*
1044 4 (1) (1982) 31–40.
- 1045 [43] H. French, Fatigue and the hardening of steels, *Transactions of the American Society for Steel*
1046 *Treating* 21 (1933) 899–946.
- 1047 [44] B. Langer, Fatigue failure from stress cycles of varying amplitude, *Journal of Applied Mechanics*
1048 4 (4) (1937) A160–A162.
- 1049 [45] A. Fatemi, L. Yang, Cumulative fatigue damage and life prediction theories: a survey of the
1050 state of the art for homogeneous materials, *International Journal of Fatigue* 20 (1) (1998) 9–34.
- 1051 [46] L. Pook, *Why Metal Fatigue Matters*, Springer, 2007.
- 1052 [47] D. C. Poirel, Random dynamics of a structurally nonlinear airfoil in turbulent flow, Ph.D. thesis
1053 (2001).
- 1054 [48] S. K. Kumar, S. Sarkar, S. Gupta, Multiplicative noise induced intermittency in maps, *Inter-*
1055 *national Journal of Non-Linear Mechanics* 117 (2019) 103251.

- 1056 [49] J. Venkatramani, V. Nair, R. Sujith, S. Gupta, S. Sarkar, Multi-fractality in aeroelastic response
1057 as a precursor to flutter, *Journal of Sound and Vibration* 386 (2017) 390–406.
- 1058 [50] V. Nair, G. Thampi, S. Karuppusamy, S. Gopalan, R. Sujith, Loss of chaos in combustion
1059 noise as a precursor of impending combustion instability, *International journal of spray and
1060 combustion dynamics* 5 (4) (2013) 273–290.
- 1061 [51] V. Nair, R. Sujith, Multifractality in combustion noise: predicting an impending combustion
1062 instability, *Journal of Fluid Mechanics* 747 (2014) 635–655.
- 1063 [52] V. Nair, G. Thampi, R. Sujith, Intermittency route to thermoacoustic instability in turbulent
1064 combustors, *Journal of Fluid Mechanics* 756 (2014) 470–487.
- 1065 [53] J. Venkatramani, V. Nair, R. Sujith, S. Gupta, S. Sarkar, Precursors to flutter instability by
1066 an intermittency route: a model free approach, *Journal of Fluids and Structures* 61 (2016)
1067 376–391.
- 1068 [54] C. Braccresi, F. Cianetti, G. Lori, D. Pioli, An equivalent uniaxial stress process for fatigue life
1069 estimation of mechanical components under multiaxial stress conditions, *International Journal
1070 of Fatigue* 30 (8) (2008) 1479–1497.
- 1071 [55] A. Carpinteri, M. De Freitas, A. Spagnoli, *Biaxial/Multiaxial fatigue and fracture*, Elsevier,
1072 ESIS Publication, 2003.
- 1073 [56] P. A. Brodtkorb, P. Johannesson, G. Lindgren, I. Rychlik, J. Ryden, E. Sjö, et al., Wafo-a
1074 matlab toolbox for analysis of random waves and loads, in: *The tenth international offshore
1075 and polar engineering conference*, International Society of Offshore and Polar Engineers, 2000.
- 1076 [57] M. Amoozgar, R. Ajaj, J. Cooper, The effect of elastic couplings and material uncertainties on
1077 the flutter of composite high aspect ratio wings, *Journal of Fluids and Structures* 108 (2022)
1078 103439.